
White Rose Research Online

eprints@whiterose.ac.uk
https://eprints.whiterose.ac.uk
Universities of Leeds, Sheffield and York

Deposited via The University of Leeds.

White Rose Research Online URL for this paper:
https://eprints.whiterose.ac.uk/id/eprint/110319/

Version: Published Version

Article:
Weiss, JR, Brooks, BA, Foster, JH et al. (2016) Isolating active orogenic wedge deformation in the southern Subandes of Bolivia. Journal of Geophysical Research: Solid Earth, 121 (8). pp. 6192-6218. ISSN: 2169-9356

https://doi.org/10.1002/2016JB013145

© 2016, American Geophysical Union. Reproduced in accordance with the publisher's self-archiving policy.

Reuse
Items deposited in White Rose Research Online are protected by copyright, with all rights reserved unless indicated otherwise. They may be downloaded and/or printed for private study, or other acts as permitted by national copyright laws. The publisher or other rights holders may allow further reproduction and re-use of the full text version. This is indicated by the licence information on the White Rose Research Online record for the item.

Takedown
If you consider content in White Rose Research Online to be in breach of UK law, please notify us by emailing eprints@whiterose.ac.uk including the URL of the record and the reason for the withdrawal request.



AGU PUBLICATIONS

JGR

Journal of Geophysical Research: Solid Earth

RESEARCH ARTICLE
10.1002/2016JB013145

Key Points:
- A new interseismic GPS velocity field for the central Andean backarc includes a correction associated with subduction zone earthquakes
- The velocity field reveals along-strike changes in the deformation character of the backarc orogenic wedge
- The wedge loading rate, décollement locked width, and slipping-to-locked transition depth decrease by a factor of ~2 from north to south

Supporting Information:
- Supporting Information S1

Correspondence to:
J. R. Weiss,
J.R.Weiss@leeds.ac.uk

Citation:
Weiss, J. R., et al. (2016), Isolating active orogenic wedge deformation in the southern Subandes of Bolivia, *J. Geophys. Res. Solid Earth*, *121*, 6192–6218, doi:10.1002/2016JB013145.

Received 4 MAY 2016
Accepted 25 JUL 2016
Accepted article online 29 JUL 2016
Published online 25 AUG 2016

©2016. American Geophysical Union. All Rights Reserved.

Isolating active orogenic wedge deformation in the southern Subandes of Bolivia

Jonathan R. Weiss[1,2,3], Benjamin A. Brooks[4], James H. Foster[3], Michael Bevis[5], Arturo Echalar[6], Dana Caccamise[5], Jacob Heck[5], Eric Kendrick[5], Kevin Ahlgren[7], David Raleigh[5], Robert Smalley Jr.[8], and Gustavo Vergani[9]

[1]Department of Geology and Geophysics, University of Hawai'i at Mānoa, Honolulu, Hawaii, USA, [2]Now at COMET, School of Earth and Environment, University of Leeds, Leeds, UK, [3]Hawai'i Institute of Geophysics and Planetology, University of Hawai'i at Mānoa, Honolulu, Hawaii, USA, [4]U.S. Geological Survey Earthquake Science Center, Menlo Park, California, USA, [5]School of Earth Sciences, Ohio State University, Columbus, Ohio, USA, [6]Instituto Geográfico Militar, La Paz, Bolivia, [7]Land Surveying/Mapping Sciences, Saint Cloud State University, St. Cloud, Minnesota, USA, [8]Center for Earthquake Research and Information, University of Memphis, Memphis, Tennessee, USA, [9]Pluspetrol SA, Buenos Aires, Argentina

Abstract A new GPS-derived surface velocity field for the central Andean backarc permits an assessment of orogenic wedge deformation across the southern Subandes of Bolivia, where recent studies suggest that great earthquakes ($>M_w$ 8) are possible. We find that the backarc is not isolated from the main plate boundary seismic cycle. Rather, signals from subduction zone earthquakes contaminate the velocity field at distances greater than 800 km from the Chile trench. Two new wedge-crossing velocity profiles, corrected for seasonal and earthquake affects, reveal distinct regions that reflect (1) locking of the main plate boundary across the high Andes, (2) the location of and loading rate at the back of orogenic wedge, and (3) an east flank velocity gradient indicative of décollement locking beneath the Subandes. Modeling of the Subandean portions of the profiles indicates along-strike variations in the décollement locked width (W_L) and wedge loading rate; the northern wedge décollement has a W_L of ~100 km while accumulating slip at a rate of ~14 mm/yr, whereas the southern wedge has a W_L of ~61 km and a slip rate of ~7 mm/yr. When compared to Quaternary estimates of geologic shortening and evidence for Holocene internal wedge deformation, the new GPS-derived wedge loading rates may indicate that the southern wedge is experiencing a phase of thickening via reactivation of preexisting internal structures. In contrast, we suspect that the northern wedge is undergoing an accretion or widening phase primarily via slip on relatively young thrust-front faults.

1. Introduction

The gently dipping fault planes ("décollements") beneath active orogenic wedges host some of the largest earthquakes on Earth [*Kanamori*, 1977; *Lay and Bilek*, 2007]. The 2004 Sumatra-Andaman (M_w 9.2), 2010 Maule (M_w 8.8), and 2011 (M_w 9.0) Tohoku earthquakes are three recent examples where rupture of the shallow megathrust beneath the submarine accretionary wedge resulted in a destructive tsunami [*Fujiwara et al*., 2011; *Lay et al*., 2005; *Vigny et al*., 2011]. In addition to oceanic subduction zones, décollements underlying subaerial orogenic wedges at plate boundaries and within continental interiors are also capable of generating large thrust earthquakes [*England and Jackson*, 2011; *Hubbard et al*., 2015]. Examples include the 1999 Chi-Chi, Taiwan (M_w 7.6), 2008 Wenchuan, China (M_w 7.9), historical great earthquakes along the Himalayan thrust front [*Bollinger et al*., 2014; *Hubbard and Shaw*, 2009; *Kao and Chen*, 2000; *Sapkota et al*., 2013], and the recent 2015 Ghorka, Nepal (M_w 7.8) event, which ruptured a previously locked portion of the main basal décollement but did not propagate to the Himalayan thrust front [*Avouac et al*., 2015; *Elliott et al*., 2016; *Lindsey et al*., 2015].

Although indispensable for investigating the basic mechanics and forcing mechanisms of orogenic wedge deformation, the critical wedge theory [e.g., *Dahlen et al*., 1984; *Davis et al*., 1983; *Whipple*, 2009; *Whipple and Meade*, 2004] is limited in its ability to address incremental fault slip processes acting over short to intermediate seismotectonic timescales, including the wedge earthquakes described above. Investigating the seismotectonics of wedges and in particular how slip on the décollement reaches the wedge front is a relatively young field of study. Work from a limited number of locations suggests that focused wedge-front deformation characterizes many active subaerial fold-and-thrust belts [*Lavé and Avouac*, 2000; *Simoes et al*., 2007;

Weiss et al., 2015]. In contrast, the Ghorka earthquake demonstrates that slip during large thrust events may be confined to deeper portions of the décollement [*Avouac et al*., 2015]. A recent combination of critical wedge theory with dynamic rupture models has shown that fault frictional strength, stress state, and branch fault intersection angle with the décollement will control whether or not a wedge earthquake will be confined to the décollement or will propagate towards the surface [*DeDontney et al*., 2012]. Additional studies focused on the non-steady state conditions of wedges have revealed episodic wedge growth in the form of alternating cycles of wedge thickening via internal deformation on preexisting (internal) structures and wedge widening via the initiation of new frontal thrusts [*Del Castello and Cooke*, 2007; *Yagupsky et al*., 2014].

Despite these advances, first-order questions remain regarding the forces that drive active wedge deformation. For example, what provides the push at the back of an active wedge and what are the slip rates on the basal décollements? Do these attributes vary in space and time and can they be quantified to better understand wedge boundary conditions? One approach researchers have adopted to gain insights in to the large-scale forces that drive continental deformation uses surface velocity gradients and a thin sheet model of viscous fluid flow to describe the bulk behavior of the lithosphere [*England and McKenzie*, 1982; *England and Molnar*, 1997; *Houseman and England*, 1986; *Lamb*, 2000]. An important outcome of the thin viscous sheet approximation is the hypothesis that variations in crustal thickness or related surface topography generate buoyancy forces that can drive the kinematics of large-scale deformation [*England and Jackson*, 1989]. Maximum gradients in surface velocity-derived buoyancy forces that parallel the regional topographic gradients provide strong evidence for the fluid-like behavior of deforming regions [*England and Molnar*, 1997; *Lamb*, 2000].

Over the past few decades, as high precision Global Positioning System (GPS) time series lengthen [e.g., *Lin et al*., 2013; *Reilinger et al*., 2006; *Segall and Davis*, 1997; *Tregoning et al*., 2013; *Vigny et al*., 2005; *Wang et al*., 2012] and satellite radar interferometry emerges as a well-established technique for measuring surface displacements [e.g., *Bürgmann et al*., 2000; *Simons*, 2007; *Wright*, 2002], it has become possible to investigate the kinematics of crustal deformation at unprecedented temporal and spatial resolutions. A natural outcome of these advances in space-based techniques is to ask if we can use the resultant surface displacement fields to investigate crustal deformation at levels similar to detailed geologic interpretations (i.e., structural cross sections), which reveal complicated subsurface geometries including duplexes, multiple detachment levels, fault propagation folds, etc. [e.g., *McQuarrie*, 2002; *Poblet and Lisle*, 2011; *Suppe and Medwedeff*, 1990; *Yue et al*., 2005]. For example, how do the large-scale forces driving continental deformation interact with the individual structures?

The Andes have served as a particularly attractive target for crustal deformation studies primarily because the highly seismogenic plate boundary along the western margin of the mountains provides the opportunity to investigate all aspects of the earthquake deformation cycle [*Wang et al*., 2012]. The steadily accumulating deformation that produces mountain ranges can also be investigated in the Andes. The southern Subandes (SSA) of Bolivia, comprising the east flank of the central Andean plateau, are a classic fold-and-thrust belt [*Davis et al*., 1983] with well-known structures and deformational timing, making them an excellent target for active orogenic wedge investigations [*Brooks et al*., 2003, 2011; *Echavarria et al*., 2003; *Kendrick et al*., 2006; *McQuarrie*, 2002; *Mugnier et al*., 2006; *Uba et al*., 2009; *Weiss et al*., 2015].

Norabuena et al. [1998] and *Bevis et al*. [2001] presented some of the first GPS-derived velocity fields for the central Andean backarc. Both described a localized velocity gradient across the Subandes and *Bevis et al*. [2001] suggested the gradient represents a shallow décollement underlying the Subandean range that is freely slipping toward the mountain interior and locked near the thrust front. However, due to the limited GPS data available at the time, the authors did not attempt to model details of the locking. Subsequently, *Brooks et al*. [2011] presented and modeled a denser backarc GPS network, which reveals a strong east flank velocity gradient, and suggested that the up-dip portion of the décollement underlying the wedge is locked downdip for ~85–100 km, while the downdip portion of the décollement beneath the high Andes is accumulating slip at a rate of ~10 mm/yr. Despite the low levels of modern and historical seismicity, the authors propose that a single strain-releasing event, rupturing the entire décollement locked width, could generate an earthquake of $> M_w$ 8.5 on average every thousand years.

To further advance our understanding of the seismotectonics of orogenic wedge deformation in general and the SSA in particular, we need to derive accurate surface displacement fields. Across the central

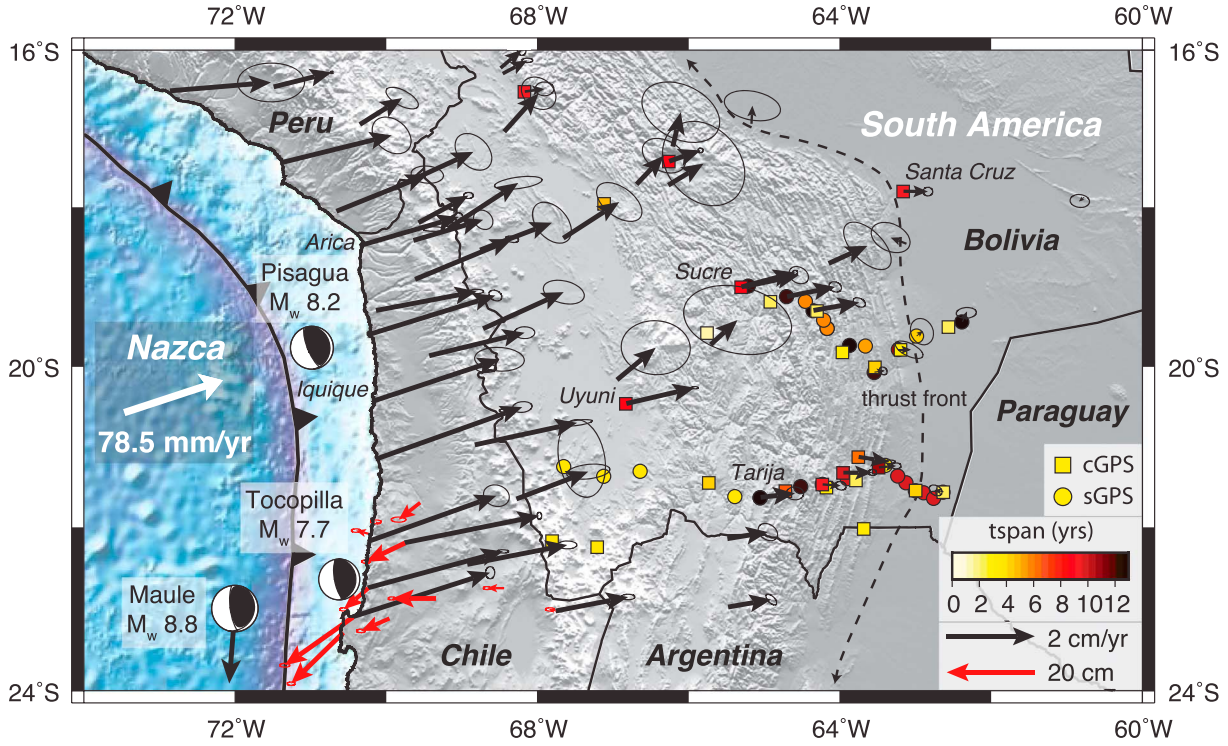

Figure 1. Interseismic GPS velocity field in a South America-fixed reference frame based on GPS sites that existed prior to the 2007 M_w 7.7 Tocopilla, Chile, earthquake with 95% confidence ellipses overlain on Shuttle Radar Topographic Mission (SRTM) topography (gray scale) and global predicted bathymetry (blue scale). Site velocities are a combination of results from this study and *Kendrick et al.* [2001] Also shown are focal mechanisms for three recent subduction zone earthquakes that affected the backarc and near-field Tocopilla earthquake horizontal coseismic displacement vectors in red from *Bejar-Pizarro et al.* [2010]. Bolivia GPS network sites are color coded by the length of time the site has been in operation. Symbols without an associated velocity vector represent sites that did not exist prior to the Tocopilla earthquake. The offshore location of the Chile trench is shown with a heavy black barbed line. The heavy white vector indicates the direction and magnitude of Nazca-South America plate convergence according to NUVEL-1A. The black dashed line indicates the approximate position of the deformation front at the eastern edge of the Andes. cGPS = continuous GPS site; sGPS = roving/campaign GPS site.

Andean backarc a significant challenge relates to isolating the strain associated with orogenic processes from the much larger elastic signals associated with the forearc and subduction zone plate boundary [*Bevis et al.*, 2001]. The SSA lie over 500 km to the east of the Nazca-South America plate boundary (Figure 1); previously, this was thought to be far enough away that locking of the main plate interface does not dominate the crustal deformation signal [e.g., *Bevis et al.*, 2001; *Brooks et al.*, 2011; *Lamb*, 2000].

Almost two decades have passed since publication of the first geodetic results from the central Andes [e.g., *Bevis et al.*, 2001; *Brooks et al.*, 2003; *Kendrick et al.*, 2006; *Norabuena et al.*, 1998]. Now that more GPS data are available for the region and in the aftermath of numerous large submarine subduction zone earthquakes including the 2007 M_w 7.7 Tocopilla, 2010 M_w 8.8 Maule, 2014 M_w 8.2 Pisagua, and 2015 M_w 8.3 Illapel, Chile, earthquakes [*Delouis et al.*, 2009; *Hayes et al.*, 2014; *Moreno et al.*, 2010; *Schurr et al.*, 2014, 2012; *Ye et al.*, 2015] we are better equipped to reexamine the effect of forearc earthquakes on the backarc velocity field and to assess locking and strain accumulation rates on the décollement beneath the active backarc orogenic wedge.

Here we present new GPS-derived surface velocities for the central Andean backarc. We find that plate boundary earthquakes at the Chile trench affect the entire backarc velocity field including sites on the adjacent foreland basin. After characterizing and removing the velocity perturbation associated with the Tocopilla earthquake, we isolate the long-term interseismic velocities and find north to south variations in the rate of contraction across the wedge and the width of the region over which the décollement becomes locked near the wedge front. Specifically, both the wedge contraction rate and the décollement locked width in the north are significantly larger than in the south.

2. Deriving the GPS Velocity Field

2.1. GPS Data Acquisition and Processing

The GPS data used in this study come from sites that are part of large regional geodetic networks, some of which have been in place since the 1990s, including the Central Andes Project [*Bevis et al*., 1999; *Brooks et al*., 2003; *Kendrick et al*., 2001] and the South America-Nazca Plate Motion Project [*Norabuena et al*., 1998]. These networks include a mix of continuously operating GPS (cGPS) sites and survey-mode GPS (sGPS) sites that are ideally occupied for a minimum of 36–48 h over consecutive days at 1 to 2 year intervals (Figure 1).

Brooks et al. [2011] provide GPS-based velocity estimates for central Andean backarc GPS sites installed from 2000 to 2003 with a total time span of 3 or more years. Here we improve on the *Brooks et al*. [2011] velocity field by including ~4 years of additional cGPS data and sGPS data collected during site reoccupations in 2011, 2012, and 2013. We also reoccupied a subset of backarc sGPS sites in mid-2014 in response to the 2014 M_w 8.2 Pisagua, Chile, earthquake (Figure 1).

The vast majority of the velocity estimates presented in *Brooks et al*. [2011] are derived from sGPS sites, which have larger positional uncertainties than cGPS sites due to their short occupation times and susceptibility to errors such as those associated with equipment setup [*Bevis et al*., 1997]. In contrast, cGPS data-derived velocities are more accurate due to the massive averaging of their daily network solutions and because the data are time continuous permitting the recognition of real and artificial jumps and removal of the latter. Our analysis includes data from ~10 new cGPS sites established across the backarc since 2009. We also include data from Altiplano and foreland basin sGPS sites established in 2007 and 2009 and occupied an average of 3 times. These newer sGPS sites are not included in the *Brooks et al*. [2011] analysis. We typically consider data from cGPS sites established for 3 years or more and sGPS sites with three or more occupations and a total time span greater than 3 years (Table 1). We also include some shorter time span (2–3 years) cGPS sites recognizing that their position and velocity uncertainties are larger than the longer-lived sites. The greater length of the GPS time series combined with the addition of new sites results in improved backarc coverage compared to previous studies [*Bevis et al*., 2001; *Brooks et al*., 2011; *Norabuena et al*., 1998]. Due to difficulties associated with traversing the Subandes by vehicle, our GPS network lies essentially within reach of the northern Route 6, which connects Sucre to Camiri, and the southern Route 11, which connects Tarija to Villamontes (Figure 1). Both roads cross the Subandes in an approximately east-west direction resulting in GPS sites that lie along two wedge-crossing profiles, which we refer to as the Sucre and Tarija profiles. At their narrowest point (~63.5°W) the two sets of sites are separated by ~100 km but they are typically $>$200 km apart (Figure 1).

Our field, processing, and velocity analysis methods in South America have been described previously [*Bevis et al*., 1997, 2001, 1999; *Brooks et al*., 2003, 2011; *Kendrick et al*., 2001, 2003, 2006, 1999]. To summarize, for each daily solution we process all the available data using GAMIT [*King and Bock*, 2000], which estimates the 3-D relative position of ground stations and satellite orbits and GLOBK [*Herring*, 2000], which merges the daily regional with global solutions for International Global Navigation Satellite Systems Service (IGS) sites. Since we are interested primarily in regional deformation, we refrain from the global stacking common to large-scale scale plate motion studies and instead stack only stations on the South American and Nazca plates and a few sites on adjacent plates and minimize motions of stations located on the stable core of the South American craton. We express our velocities in a craton-fixed reference frame with horizontal and vertical velocities of less than 1 mm/yr (Table S1 and Figure S1 in the supporting information). Specifically, we use 44 cGPS stations primarily located in Brazil to create the horizontal reference frame. These sites have a total RMS horizontal velocity of 0.66 mm/yr. The total RMS velocity of the 35 sites used to constrain the vertical reference frame is 0.94 mm/yr. We estimate central Andean site velocities in this stable reference frame by performing linear fits through the daily positions for each station in the network while minimizing the misfit across the entire network. Below we describe a few additional modifications to our velocity estimation approach.

2.2. Seasonal Signal Estimation

Seasonal perturbations due to climate-driven deformation of the solid earth affect the GPS time series and must be taken in to account when calculating site velocities [*Bevis and Brown*, 2014; *Blewitt and Lavallée*, 2002] (Figures 2 and S1), particularly when sGPS site occupations were performed at different times of the year. These changes in lithospheric loading due primarily to surface water, snow, and ice are of particular concern in our study area, which lies between the Amazon rainforest to the northeast and glaciated portions of the Andes to the west. Pronounced rainfall gradients across and along the Andean backarc [*Strecker et al*., 2007] also

Table 1. Corrected GPS Site Interseismic Velocities[a]

Stnm	sc	Lon	Lat	V_n	V_e	V_u	sigNs	sigEs	sigUs	sigNc	sigEc	sigUc	neCor	tspan
0B54	s	−64.1673	−19.5233	1.02	8.12	0.10	0.17	0.77	1.15	0.34	1.30	1.06	−0.56	5.88
0B85	s	−64.4549	−19.1819	1.86	10.14	−0.27	0.71	0.65	2.23	1.40	0.76	2.41	−0.38	5.88
0B87	s	−64.2072	−19.4211	1.18	8.46	−0.09	0.26	0.41	1.14	0.48	0.60	1.09	−0.55	5.88
0B89	s	−63.6577	−19.7424	0.27	4.08	1.44	0.69	0.33	0.91	0.93	0.66	0.92	−0.16	5.20
ASLO	s	−64.1673	−19.5232	0.59	7.85	−0.11	0.28	0.17	0.43	1.33	0.85	0.50	−0.48	12.82
BLPZ	c	−68.1683	−16.5299	0.52	4.26	2.70	0.01	0.01	0.03	0.15	0.20	0.56	−0.21	9.17
BOQN	c	−63.1947	−19.7907	0.65	1.38	2.13	0.03	0.04	0.15	0.25	0.33	0.77	−0.22	3.36
BPDL	c	−64.2999	−19.3044	1.37	9.57	0.19	0.11	0.08	0.27	1.64	0.53	1.54	−0.35	2.24
BPLB	c	−63.7838	−21.4167	0.22	4.44	3.14	0.06	0.08	0.24	0.54	0.72	1.08	−0.25	2.32
BPSC	c	−62.6297	−21.5620	0.00	−1.06	2.17	0.05	0.07	0.19	0.40	0.42	0.83	−0.21	2.32
BRCH	c	−62.5611	−19.5053	1.73	0.48	1.70	0.07	0.10	0.33	0.67	1.26	0.97	−0.22	2.32
BTRC	c	−64.9149	−19.1886	2.34	11.13	0.97	0.05	0.09	0.22	0.54	0.68	0.94	−0.20	2.31
CAGA	s	−63.2242	−19.7902	0.07	2.34	0.30	0.15	0.17	0.56	0.26	0.36	0.93	−0.30	10.85
CAMR	c	−63.5334	−20.0102	0.21	1.65	2.42	0.03	0.09	0.12	0.33	2.02	0.60	−0.14	4.33
CBMB	c	−66.2588	−17.4166	2.46	7.00	1.10	0.02	0.02	0.03	0.77	0.37	3.43	−0.23	8.39
CCDO	s	−62.3808	−19.4391	1.93	0.93	1.13	0.12	0.17	0.36	0.33	0.56	0.38	−0.09	12.81
CCYA	s	−65.0479	−21.6304	3.03	8.68	4.66	0.19	0.43	0.79	0.35	0.74	0.76	−0.49	9.99
CHYY	s	−63.8694	−19.7364	0.32	5.52	−15.97	0.11	0.22	5.82	0.20	0.59	11.14	−0.34	12.83
CMRI	s	−63.5425	−20.0712	0.19	2.06	−6.71	0.07	0.10	1.17	0.43	0.51	5.59	−0.33	12.14
COCI	s	−66.6405	−21.3035	3.33	14.37	2.09	0.63	0.13	1.91	0.74	0.40	1.76	−0.37	3.69
COLO[p]	c	−67.8040	−22.1674	3.58	17.55	3.05	0.02	0.04	0.10	0.18	0.28	0.72	−0.11	3.96
CULK	s	−67.1211	−21.3657	3.58	15.82	1.82	0.23	0.63	1.26	0.28	0.82	1.18	−0.69	3.71
DRDO	s	−64.3498	−19.2968	1.87	10.37	−0.47	0.09	0.11	6.70	0.27	0.32	14.83	−0.34	12.81
ENRI[b]	s	−64.2280	−21.4678	1.45	3.78	0.06	0.16	0.30	0.24	0.19	0.73	0.13	0.13	2.84
GLPE	c	−64.1754	−21.5065	1.20	5.01	1.28	0.22	0.35	1.40	2.03	2.11	2.97	−0.29	3.36
IBOB	c	−62.9945	−21.5427	0.11	−0.66	2.76	0.03	0.04	0.12	0.32	0.31	0.54	−0.24	4.38
LPTS[g]	c	−65.7538	−19.5820	3.08	12.44	0.84	0.26	0.33	0.83	2.12	2.08	2.81	−0.20	1.36
M007	s	−63.9008	−21.3953	0.19	5.60	2.20	0.17	0.18	0.75	0.33	0.40	0.84	−0.16	9.88
M009	s	−62.8877	−21.5702	0.35	−0.33	2.68	0.19	0.20	0.30	0.30	1.19	0.21	0.13	9.90
M010	s	−62.7584	−21.6409	0.47	−0.52	2.55	0.24	0.14	0.37	0.44	0.74	0.49	0.01	9.90
M011	s	−63.1210	−21.4456	0.31	−0.29	3.12	0.06	0.39	0.43	0.12	1.07	0.42	0.18	9.89
M012	s	−63.2295	−21.3620	−0.01	−0.10	2.96	0.46	0.20	0.61	0.65	0.75	0.58	−0.03	9.89
MARG	c/s	−63.7520	−21.1291	−1.13	7.00	−1.02	0.10	0.12	0.15	0.42	0.56	0.52	−0.21	6.23
MGDO	c	−63.9623	−19.8223	0.35	5.74	1.08	0.03	0.05	0.14	0.29	0.41	0.70	−0.23	3.36
NTRS	s	−64.2283	−21.4676	1.19	5.43	2.08	0.28	0.81	0.32	0.33	1.30	0.34	−0.13	9.22
PBLA	s	−65.3820	−21.6149	3.12	9.83	4.26	0.56	1.07	1.84	0.60	1.41	1.73	−0.46	3.67
PBOL	s	−62.6294	−21.5619	0.05	−0.60	2.48	0.27	1.10	0.35	0.45	1.44	0.34	0.22	9.90
PLLO	s	−64.5179	−21.4956	2.00	8.56	4.51	0.38	0.29	0.47	0.14	0.36	0.95	−0.30	12.06
SALA	s	−62.9849	−19.6186	0.94	1.05	−2.13	0.50	0.38	2.27	1.62	0.81	2.35	−0.16	4.23
SANA	s	−67.6520	−21.2470	3.90	17.54	1.56	0.15	0.37	1.83	0.42	0.63	1.57	−0.54	3.73
SCRZ	c	−63.1597	−17.7968	−0.01	5.40	−1.68	0.02	0.03	0.04	1.75	1.11	4.81	−0.18	9.38
SUCE	c	−65.3026	−19.0062	3.19	12.27	−0.08	0.02	0.03	0.04	0.25	0.25	0.93	−0.23	8.35
SUCR[b]	s	−65.2060	−18.9921	1.99	11.56	0.98	0.25	0.56	1.34	0.42	0.79	1.55	−0.36	12.07
TARI	s	−65.0479	−21.6307	3.08	8.52	4.02	0.15	0.29	1.01	0.65	0.68	1.10	−0.24	12.82
TPYO	c/s	−63.9545	−21.3247	0.08	6.63	2.38	0.28	0.15	0.24	1.35	0.66	0.60	−0.17	9.97
TPZA	c	−65.7299	−21.4482	3.95	10.76	2.97	0.06	0.06	0.11	1.37	2.45	5.78	−0.10	4.05
TRJA	c	−64.7165	−21.5495	2.54	6.90	3.46	0.02	0.03	0.08	0.59	0.47	0.69	−0.31	6.87
URUS	c	−67.1144	−17.9528	2.74	9.58	2.13	0.03	0.03	0.07	0.34	0.32	0.74	−0.25	4.57
UTUR[p]	c	−67.2055	−22.2420	3.77	15.15	2.85	0.02	0.03	0.08	0.37	0.35	0.58	−0.24	3.96
UYNI	c	−66.8260	−20.4659	3.66	15.30	−0.60	0.02	0.02	0.02	0.84	0.43	2.11	−0.13	8.34
VMON	c	−63.4836	−21.2589	0.52	3.86	0.65	0.03	0.03	0.04	1.36	0.75	2.81	−0.20	10.65
VMT3[b]	s	−63.3957	−21.2286	0.21	−0.39	−2.32	0.80	1.17	2.18	1.11	1.69	1.92	0.06	2.91
YCBA	c	−63.6800	−22.0171	0.79	3.19	2.65	0.03	0.04	0.14	0.28	0.28	0.80	−0.28	3.37
ZDNZ	s	−64.6980	−19.1234	2.20	10.88	0.11	0.06	0.14	0.21	0.23	0.43	0.43	−0.18	12.09

[a]GPS site velocities expressed relative to the stable South American plate. Stnm, station code; s, survey (sGPS) site; c, continuous (cGPS) site; c/s, former cGPS site current sGPS site; Lon, longitude; Lat, Latitude; V_n, north component of velocity (mm/yr); V_e, east component of velocity (mm/yr); V_u, up component of velocity (mm/yr); sigNs, standard north error (mm/yr); sigEs, standard east error (mm/yr); sigUs, standard up error (mm/yr); sigNc, corrected north error (mm/yr); sigEc, corrected east error (mm/yr); sigUc, corrected up error (mm/yr); neCor, northeast correlation; tspan, time span of measurement in years. [p]PLUTONS site. [g]GLISN site.
[b]Site with no post-Tocopilla observations.

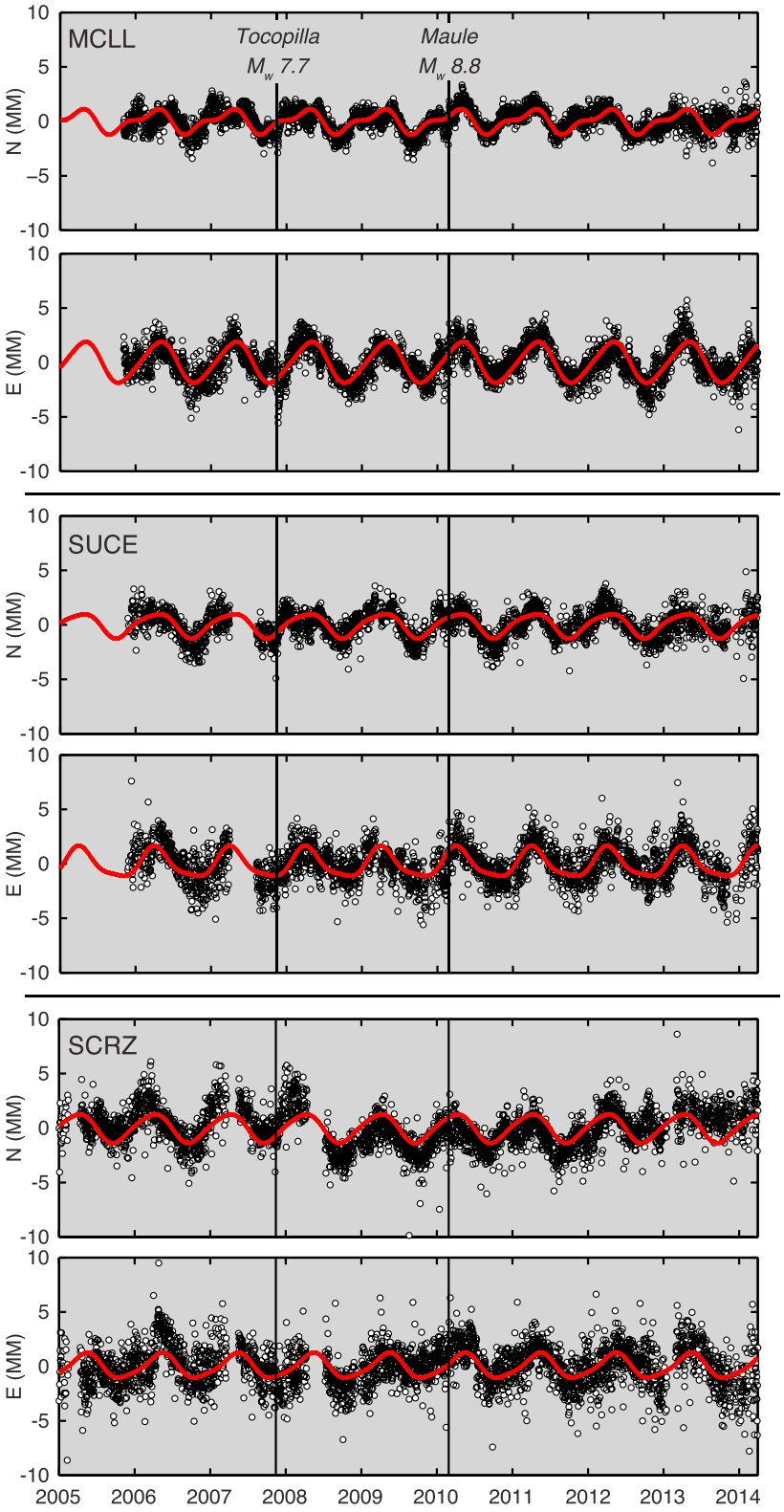

Figure 2. Examples of the seasonal perturbations for the north and east components of the GPS time series for central Andean sites located on the forearc (MCLL), backarc (SUCE), and near the front of the Subandean wedge (SCRZ). The interseismic, coseismic, and postseismic signals have been removed leaving just the seasonal component. Daily positions are shown as white circles, and the best fit sinusoidal function to the seasonal is shown in red. The up components of the time series are shown in Figure S1.

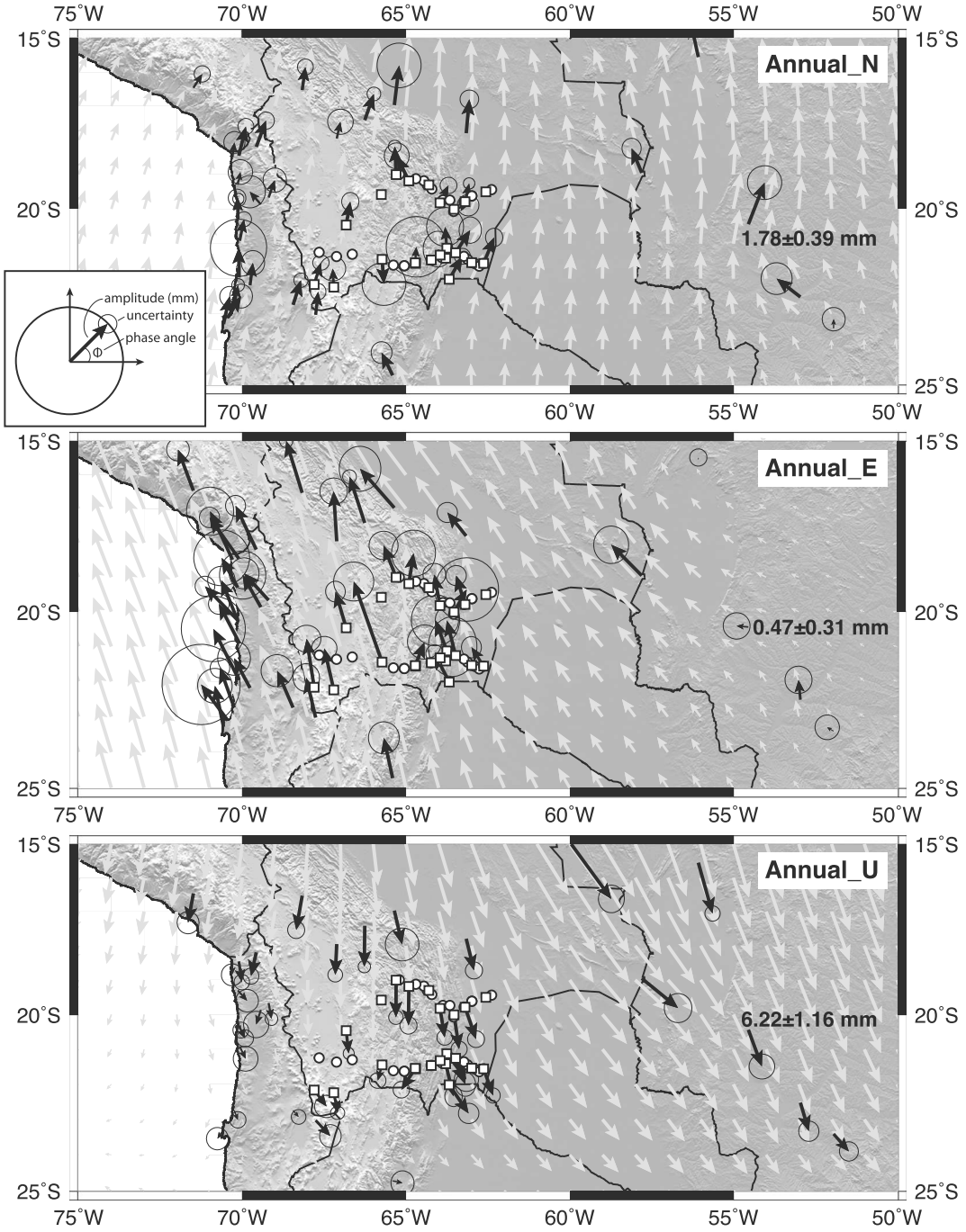

Figure 3. North, east, and up annual seasonal cycles for the central Andes. Black vectors and 2σ error ellipses are estimated directly from the cGPS time series. Gray vectors are the interpolated values. Also shown are the locations of the Bolivian cGPS and sGPS sites as white squares and circles, respectively.

contribute to the seasonal signals present in our time series. *Bevis et al.* [2005] show annual displacement cycles driven by seasonal variations in the mass of water residing in the Central Amazon Basin with peak vertical amplitudes of close to 40 mm with horizontal cycles an order of magnitude less.

We account for seasonal cycles in our GPS time series data for each of the NEU (north, east, and up) coordinates using a sinusoidal function consisting of one annual and one semiannual term [e.g., *Bevis and Brown*, 2014; *Langbein*, 2004]:

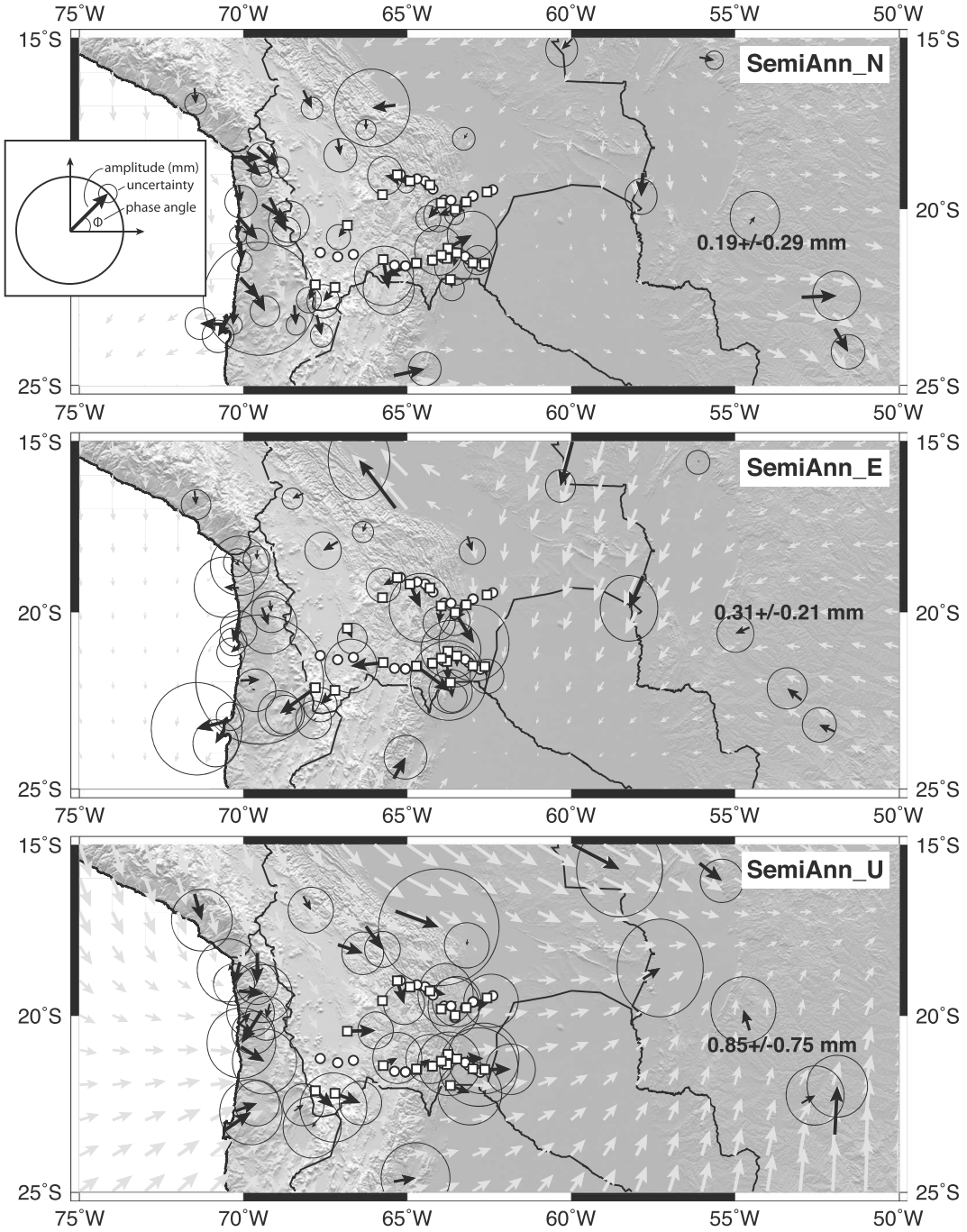

Figure 4. North, east, and up semiannual seasonal cycles for the central Andes. All symbols are the same as in Figure 3.

$$\text{seasonal}_{\text{NEU}} = \sum_{k=1}^{n_F} [s_{k_{\text{NEU}}} \sin(\omega_k t) + c_{k_{\text{NEU}}} \cos(\omega_k t)], \quad (1)$$

where s_k and c_k are the sine and cosine amplitudes at frequency ω_k and n_F is the number of frequencies or harmonics used to model the displacement cycles. For our purposes $n_F = 2$ and

$$\omega_k = \frac{2\pi}{\tau_k}, \quad \tau_1 = 1 \text{ year} \quad \text{and} \quad \tau_2 = 1/2 \text{ year}.$$

We estimate the best-fit seasonal cycle amplitudes for cGPS site time series with little to no data gaps. A number of cGPS sites do not fit these criteria and we cannot directly estimate seasonals for sGPS sites.

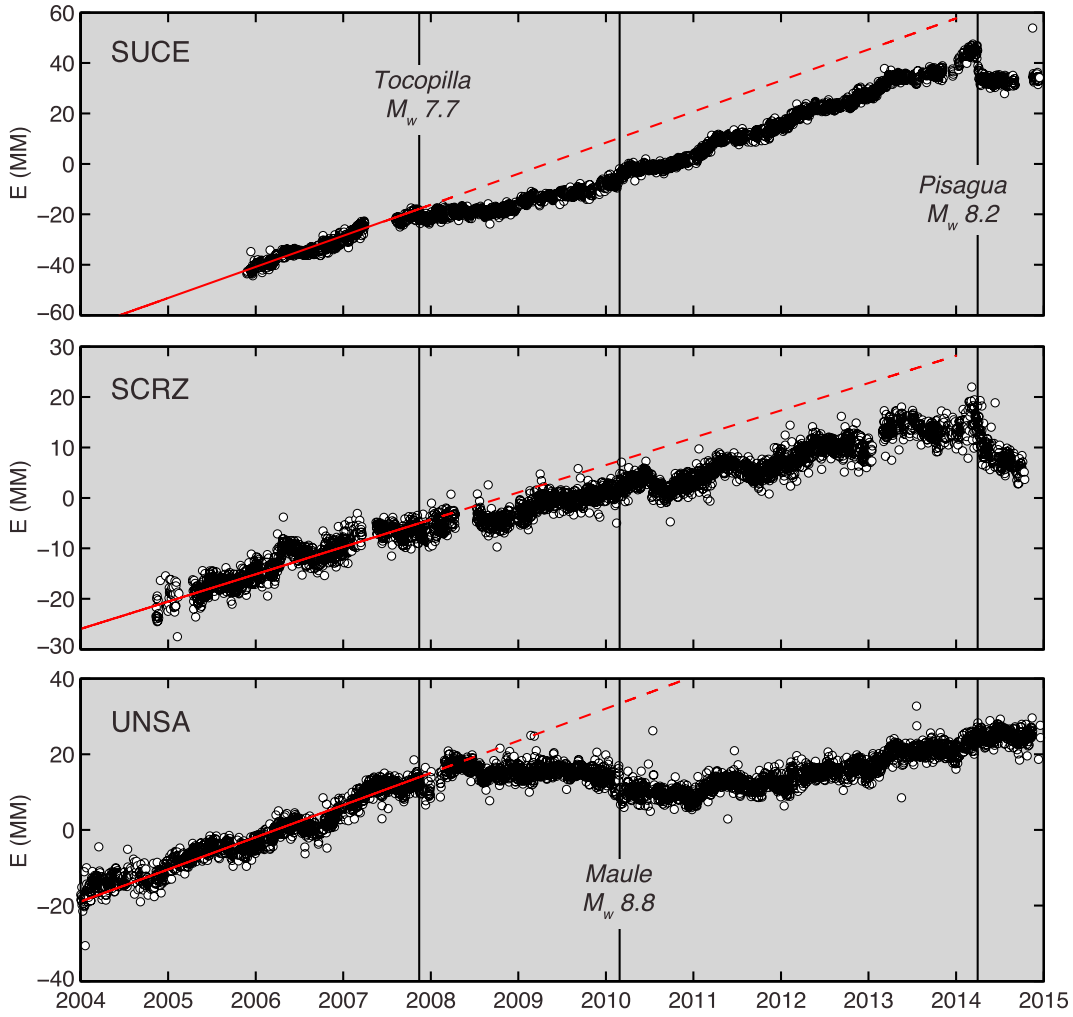

Figure 5. Eastward displacements for affected cGPS sites with the earthquake times indicated by vertical black bars. Note that the Tocopilla earthquake perturbed the time series for sites as far away as Santa Cruz, implying that the entire backarc was affected. The Maule earthquake only affected the IGS site UNSA in NW Argentina, whereas the Pisagua event affected the Bolivian sites SUCE and SCRZ. The red lines indicate a best fit velocity for the pre-Tocopilla portions of the time series and an extrapolation of this velocity beyond the time of the earthquake (red dashed) to demonstrate how the time series deviate from the prequake velocity.

We therefore interpolate the best fitting annual and semiannual amplitudes and phases for sites that do fit these criteria onto a regular grid and find that whereas a consistent regional pattern characterizes the annual component of the seasonals, the semiannual component varies between stations in an irregular, nonpredictable way (Figures 3 and 4). Based on these results, we extract only the annual component from the interpolated grid for cGPS sites without seasonal estimates, and for all sGPS sites, and we include a semiannual component only for cGPS sites where it can be estimated directly from the data.

2.3. Plate Boundary Earthquake Perturbation and Characterization

Initial analysis of the Subandean cGPS site time series revealed unexpected perturbations most noticeable in the eastward displacements at times corresponding to recent Chilean earthquakes and in particular the 14 November 2007 M_w 7.7 Tocopilla event [*Delouis et al.*, 2009; *Schurr et al.*, 2012] (Figure 5). We initially noticed the perturbation as a change in velocity for the IGS cGPS site UNSA in northwestern Argentina. A velocity change at UNSA is also apparent in association with the 2010 M_w 8.8 Maule, Chile, earthquakes [*Moreno et al.*, 2010]. Subsequent analysis of the Bolivian cGPS site time

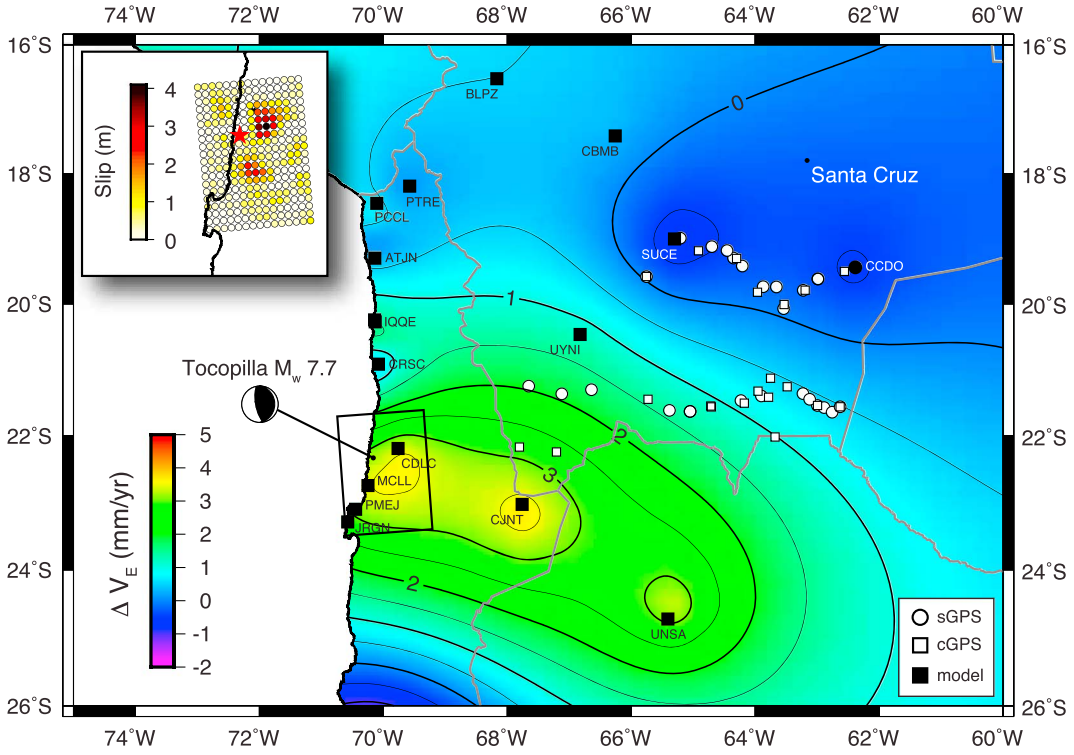

Figure 6. Simplified model of the region affect of the Tocopilla earthquake created by subtracting the best fit postquake velocity from the best fit prequake velocity for sites that existed prior to the event (black symbols) and interpolating the change in velocity (ΔV_E) across the region. Positive ΔV_E indicate a faster prequake velocity. The earthquake-induced perturbation extends across the backarc and affects the GPS network (white symbols). The small black rectangle indicates the position of the USGS slip distribution, which is shown in the inset.

series revealed a Tocopilla-related velocity field perturbation at all of the Altiplano and Subandean cGPS sites where data exist prior to the earthquake including SUCE and SCRZ (Figure 5). These two Bolivian sites were not affected by the Maule earthquake but do show clear coseismic offsets and postseismic responses associated with the 2014 M_w 8.2 Pisagua, Chile earthquake [*Hayes et al.*, 2014; *Schurr et al.*, 2014].

We find a regional pattern of postquake eastward velocity decrease when we subtract the post-Tocopilla from the pre-Tocopilla best fit velocities (Figure 6). Because the central Andean backarc region and the southern Subandean profile sites in particular were affected by the Tocopilla event, failure to recognize and account for earthquake-related transients in the GPS time series could result in inaccurate site velocity estimates (Figure 8). Therefore, one of our initial goals is to characterize the Tocopilla-related perturbation recorded in the GPS data in order to create a velocity field uncontaminated by plate boundary earthquakes. We reserve a similar examination of the Pisagua earthquake-related perturbation for a future effort and exclude post-Pisagua portions of the GPS time series from the analysis presented here.

In order to correct the backarc velocity field we assume the earthquake-affected sites will not experience a permanent change in velocity but rather eventually return to their interseismic or prequake velocity prior to the next major earthquake that is large enough to affect the central Andean backarc [*Wang et al.*, 2012]. To characterize the velocity perturbation, we adopt an empirical approach similar to recent studies of major strike-slip earthquakes [e.g., *Ergintav et al.*, 2009; *Hearn*, 2003]. GPS sites close to the earthquake epicenter in northern Chile behave in a fashion comparable to observations from other large earthquakes. This behavior includes a large coseismic offset followed by postseismic deformation in the form of superimposed rapidly and more slowly decaying transients (Figure 7). Poroelastic rebound, afterslip on or near the rupture zone, and near- and far-field viscoelastic relaxation of the upper mantle and/or lower crust are generally thought to control this behavior

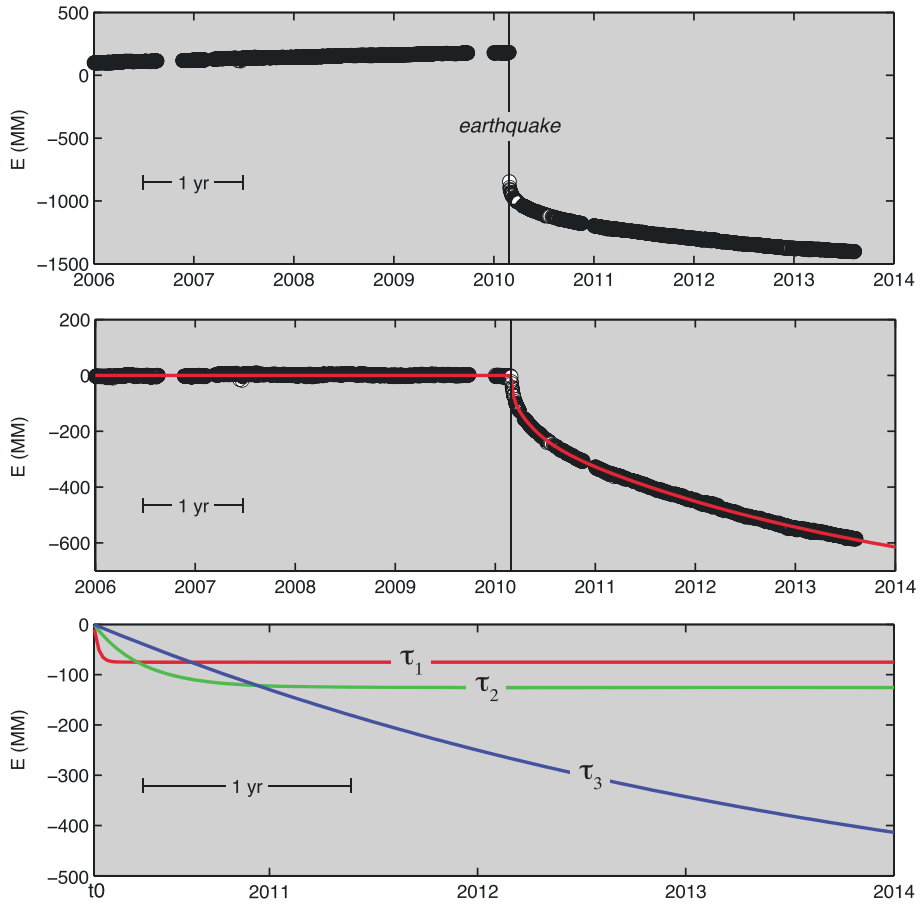

Figure 7. (top) The eastward displacement component of a typical subduction zone earthquake-affected cGPS time series from a site located close to the trench. The site is moving to the east at its interseismic velocity prior to the earthquake, which is marked by a westward coseismic offset and a postseismic decay. (middle) The same time series with the best fit interseismic velocity and coseismic step removed to illustrate the postseismic signal. (bottom) The three exponential decay terms that best fit the postseismic portion of the time series. In this and similar cases the postseismic portion of the time series can be described by the linear superposition of three exponential terms with time constants on the order of 1 to a few days (τ_1), tens to hundreds of days (τ_2), and 5–20 years (τ_3). The central Andean backarc sites are typically well described by a single exponential term with a time constant on the order of 5–10 years.

[*Barbot and Fialko*, 2010; *Bevis and Brown*, 2014; *Ergintav et al.*, 2009; *Hearn*, 2003; *Meade et al.*, 2013; *Tobita*, 2016; *Wang et al.*, 2012].

We model the NEU components of the GPS time series using a linear combination of an interseismic velocity, a coseismic step, a postseismic term with up to three characteristic time constants and the previously described seasonal term [e.g., *Bevis and Brown*, 2014]:

$$\text{model}_{\text{NEU}} = \text{interseismic}_{\text{NEU}} + \text{coseismic}_{\text{NEU}} + \text{postseismic}_{\text{NEU}} + \text{seasonal}_{\text{NEU}} \quad (2)$$

where

$$\text{interseismic}_{\text{NEU}} = a0_{\text{NEU}} + (t - t0)b_{\text{NEU}}, \quad (3)$$

where t is time, $a0_{\text{NEU}}$ are the y intercepts of best-fit lines to the prequake portions of the NEU components of the GPS time series residuals, b_{NEU} are the slopes of the best-fit lines or the interseismic/prequake velocities, $t0$ is the time of the earthquake,

$$\text{coseismic}_{\text{NEU}} = \text{coseismic\_step}_{\text{NEU}} \cdot \text{ystep} \quad (4)$$

where $\text{coseismic\_step}_{\text{NEU}}$ are the coseismic displacements measured from the GPS data, and ystep is the unit step (Heaviside) function consisting of zeroes before the earthquake and ones after the earthquake. Finally,

$$\text{postseismic}_{\text{NEU}} = \text{ystep} \sum_{i=1}^{3} \left(A_{i_{\text{NEU}}}(1 - \exp(-\text{tstep}/\tau_i))\right), \quad (5)$$

where $A_{i\mathrm{NEU}}$ are the amplitudes of the ith exponential terms, τ_i is the time constant of the ith exponential term and tstep is the time since the earthquake. Our choice of exponentials for postseismic characterization is not meant to point towards any particular underlying geophysical control on the process (e.g., viscoelastic relaxation) but rather is a computational convenience; logarithmic or spline functions, for example, can fit the data equally well [*Bevis and Brown*, 2014; *Ergintav et al*., 2009; *Hearn*, 2003].

We find that for near-field (with respect to the trench) sites in northern Chile 2–3 exponential terms with τ_1 on the order of 1 to a few days, τ_2 on the order of tens to hundreds of days, and τ_3 on the order of 5–20 years are necessary to fully describe the postseismic portion of the GPS time series (Figure 7). For middle- and far-field sites like UNSA and those across the backarc, the postseismic response is manifest as a change in velocity (Figure 8), which suggests that the timescale of the underlying deformation process is slow compared to the time that has elapsed since the Tocopilla earthquake and that our postquake observation time span of ~7 years appears to be insufficient to fully characterize the long-term regional transient behavior since the backarc GPS sites do not return to their prequake velocities [*Ergintav et al*., 2009].

We find that three exponential terms are not required to adequately describe the backarc transients due to the general lack of short-term (τ_1 and τ_2) components in a majority of the Bolivian time series. Rather, a single term with a time constant (τ_3) of ~5–10 years results in a good fit to the Subandean sites (compare Figure 5 and τ_3 in Figure 7) with the exception of SUCE (Figure 5) where a single intermediate decay term ($\tau_2 = \sim 1$ year) provides the best fit to the data. For the vast majority of our Subandean sites we simplify the postseismic parameter estimation by fixing a single decay time of 10 years and estimating the best fit long-term exponential term amplitudes (A_3; Table S1).

Our empirical characterization of the GPS time series requires two additional components: coseismic offsets and prequake/interseismic site velocities. Coseismic offsets associated with the Tocopilla earthquake are not typically observed or are minimal at the backarc cGPS sites that existed prior to the earthquake (Figure 5). The midfield Altiplano site UYNI is the only Bolivian cGPS site where we can compute a statistically significant coseismic displacement (Figure 8 and Table S1). Offsets may be present at other Bolivian sites, but data gaps around the time of the earthquake or little to no prequake data prevent us from estimating a coseismic step. Further, we have no way of directly estimating nor do we need an estimate of the Tocopilla-related coseismic offset at GPS sites established after the earthquake. Only for sites with prequake data do we attempt to estimate coseismic offsets, and only where the estimates are statistically significant (i.e., offset $> \sigma_{\mathrm{offset}}$) do we incorporate them in our analysis.

The postseismic portion of the time series can be represented as a linear combination of the interseismic velocity and the postseismic transient. Our general approach involves subtracting the seasonal signal from the GPS site time series and performing a nonlinear, least squares regression (Levenberg-Marquardt method) to find the parameters that best describe the coseismic and postseismic portions of the time series with no a priori constraints on the model parameters. For sites with prequake data (e.g., SUCE and SCRZ, Figure 5; UYNI, Figure 8), we estimate the interseismic portion of the model directly from the NEU time series and search for the best-fit coseismic steps and long-term exponential decay amplitudes.

For sites that did not exist prior to the earthquake (e.g., COLO and COCI; Figure 8), and with only a limited postseismic time window, we are unable to robustly isolate these two components. Instead, to characterize the postseismic transients for sites without prequake data, we use an a priori estimate of the prequake surface velocity. We estimate an a priori interseismic velocity field using sites with sufficient prequake data to interpolate on to a regular grid and create a map of interseismic surface velocities (Figure S3). This is a good approximation of the backarc interseismic velocity field considering the regional distribution of sites with prequake estimates and because a large megathrust earthquake had not occurred on the central Andean portion of the Chile trench for ~130 years prior to the Tocopilla and subsequent Pisagua events [*Schurr et al*., 2014, 2012]. For sites established after the Tocopilla event we extract the interseismic surface velocities from the interpolated grid and solve for the long-term exponential decay amplitudes only.

Once we have estimates for all the parameters, we subtract the coseismic and postseismic portions of the model from the GPS site time series and compute new best-fit velocities for each site (Table 1). For sites

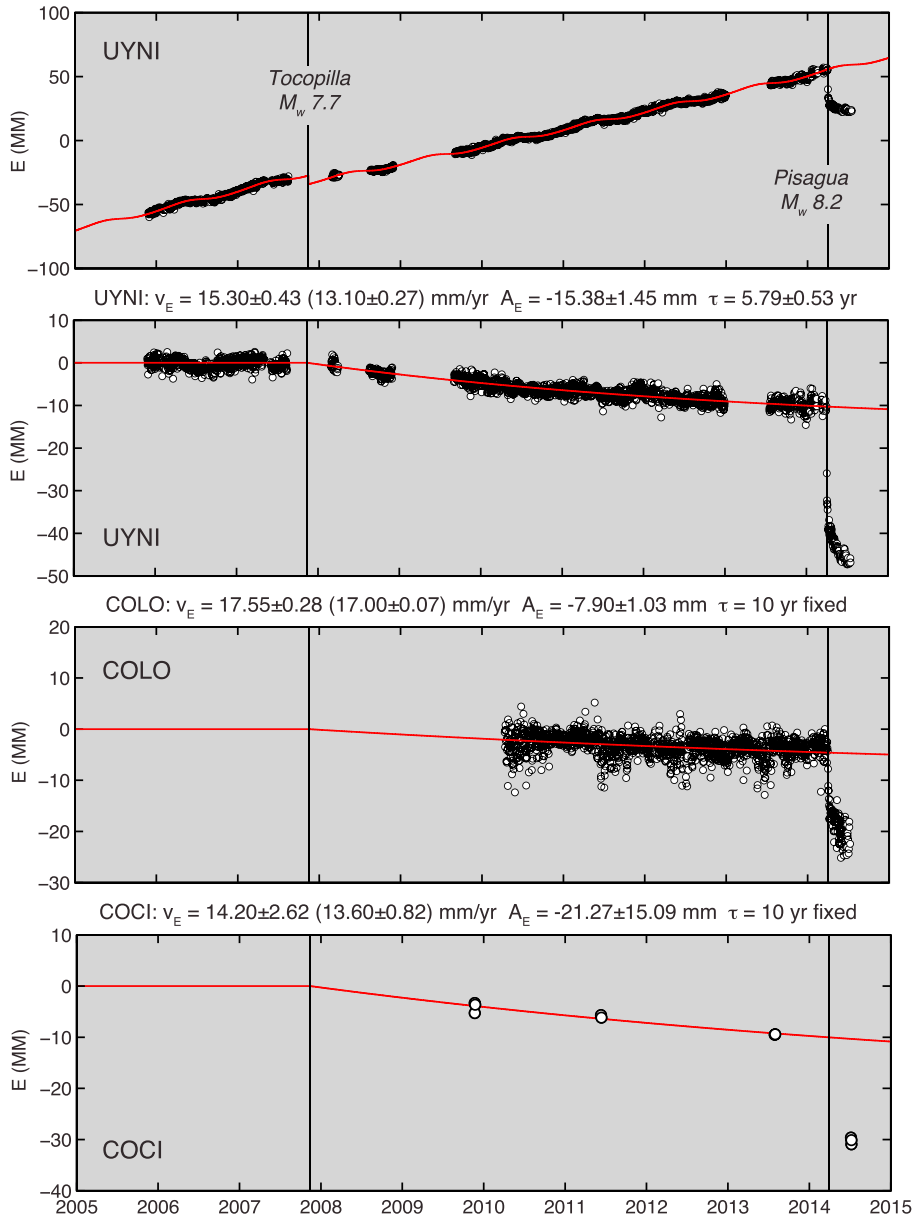

Figure 8. Examples of the eastward displacement of time series for select central Andean backarc sites and the best fit empirical models for the Tocopilla postseismic characterization. (firs panel) The daily positions for the Altiplano/Eastern Cordillera site in Uyuni, Bolivia (UYNI), and the model in red, which consists of interseismic, coseismic, postseismic, and seasonal terms. (second panel) The UYNI time series with the interseismic, coseismic, and seasonal portions removed. Remaining is the postseismic signal, which is best fit by a single exponential term with an amplitude of −15.38 mm and a decay time of 5.80 years. The correction results in an ~2 mm/yr increase in the eastward velocity. (third and fourth panels) The examples of the postseismic signal for a cGPS site (COLO) established in early 2010 and a sGPS site (COCI) first occupied in late 2009. For both cases the time constant is fixed at 10 years. For all cases we report the best fit amplitudes and velocities with the corrected errors. The uncorrected values and associated standard errors are in parentheses. The affect of the 2014 Pisagua earthquake can also be seen at each of the stations.

with prequake data the new velocities are similar to the prequake values. For sites without prequake data, the new velocity estimates mimic the interseismic values from the interpolated grid. Crucially, by adopting a conservative approach to estimating the errors, which we describe in the following section, the incorporation of a priori interseismic velocities for some sites should not unduly constrain our model towards these specific values.

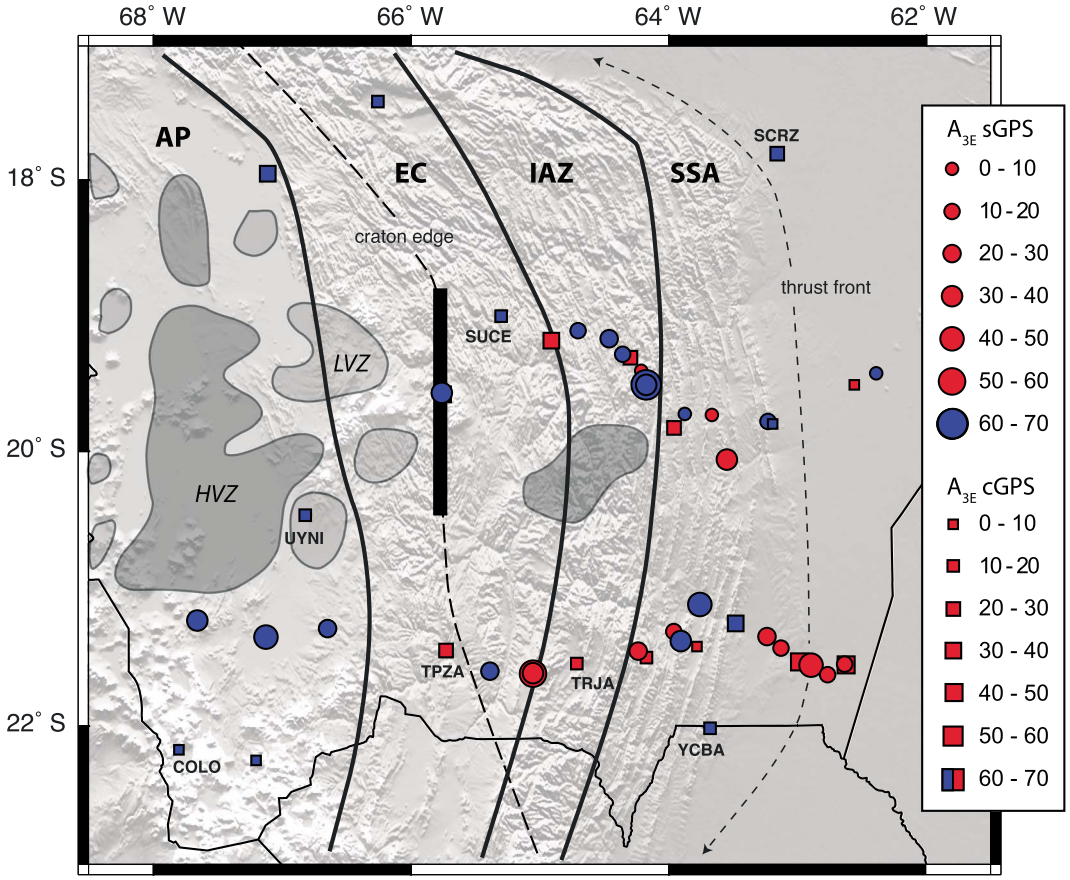

Figure 9. The best fit amplitudes for the eastern component of the exponential terms used in the Tocopilla earthquake characterization. Squares and circles correspond to cGPS and sGPS sites, respectively. Red and blue symbols indicate sites with positive and negative postseismic amplitudes, respectively. Also shown for comparison are seismological results from *Beck and Zandt* [2002] including the western edge of the underthrusting Brazilian craton (black bar) and its along-strike extent (dashed line) and high and low upper mantle *P* wave velocity zones. Also shown are the approximate boundaries of the central Andean physiographic provinces (heavy black lines). HVZ = high velocity zone; LVZ = low velocity zone; AP = Altiplano; EC = Eastern Cordillera; IAZ = Interandean Zone; SSA = southern Subandes.

Figure 8 shows examples of the eastward displacements for select backarc sites where the best fit postseismic amplitudes are negative and the corrected eastward velocities are greater than the uncorrected values. We expect this behavior due to the geometry of the megathrust with respect to the backarc (Figures 1 and 6). Slip during a subduction zone earthquake like the Tocopilla and Pisagua events results in predominantly seaward coseismic displacement of the upper plate, and affected GPS sites typically record westward coseismic and postseismic motions (Figures 1, 7, and 8) [e.g., *Lin et al*., 2013]. However, the Tocopilla earthquake-related results for the central Andean backarc exhibit substantial and often unexpected variability with respect to both the sign and magnitude of the best-fit exponential decay amplitudes (Figure 9). We cannot rule out that this variability is the result of overfitting the relatively sparse sGPS data and cGPS time series that begin after the earthquake since the few cGPS sites established prior to the earthquake generally behave as expected (Figure 6). However, the confidence intervals on the postseismic parameters suggest this is not the case (Table S2), and our conservative velocity errors (see section 2.4 and Table 1) account for the possibility that our approach is inadequate. Further, the distinct characteristics of the Sucre and Tarija profiles, described in detail in section 3.2, are present in the uncorrected data and merely accentuated in the corrected data (Figure 10) lending further support to our approach and results.

We can think of a few physical factors that possibly contribute to the variability in postseismic amplitudes. First, numerical studies of postseismic relaxation using quasi-realistic rheologies (e.g., layered viscoelastic, and power law) often show variable behavior similar to our observations particularly in the far-field regions

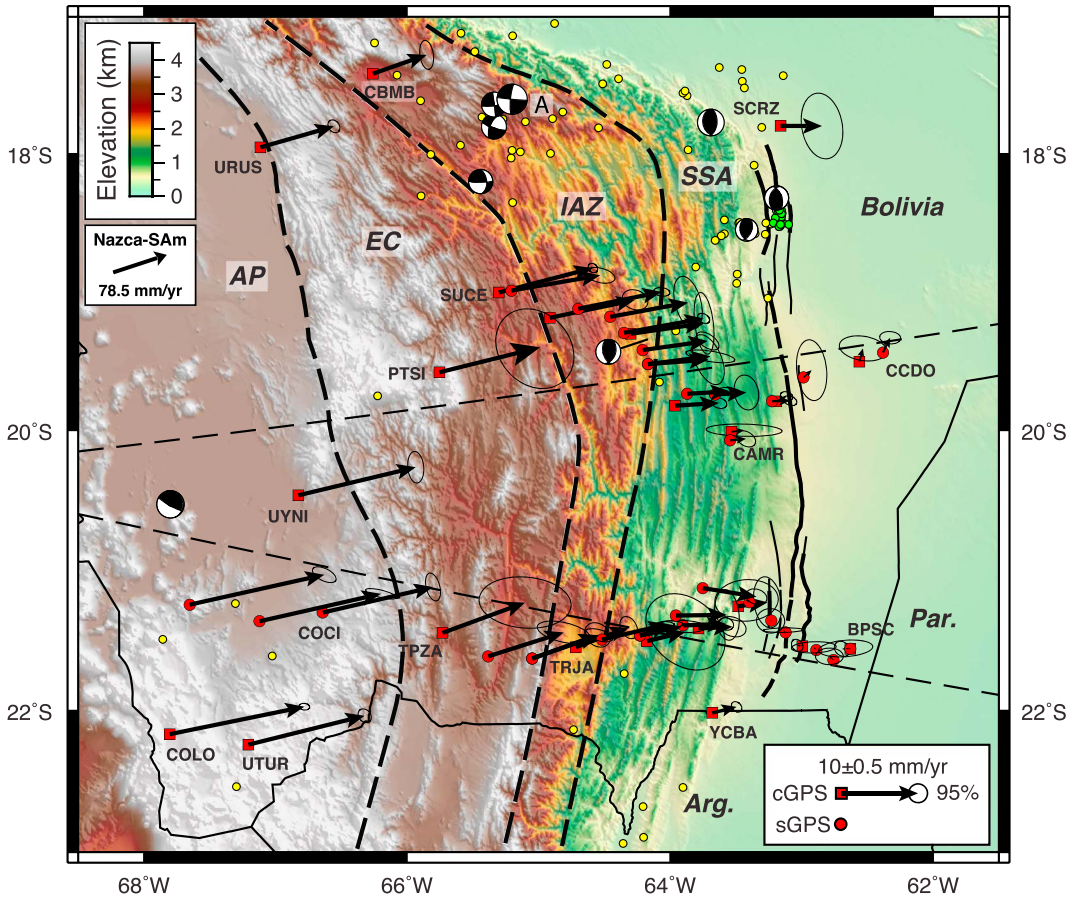

Figure 10. The new central Andean backarc velocity field with 95% confidence ellipses based on the corrected errors overlain on SRTM topography. The wedge-front Mandeyapecua thrust fault system (MTFS) from *Weiss et al.* [2015] is shown as thick and thin black lines for surface and buried faults, respectively, all of which dip to the west. Thin dashed lines indicated the location of the two wedge-crossing profiles from Figures 10 and 11 and thick black lines indicate the approximate boundaries of the major physiographic provinces. Select GPS sites are labeled with their corresponding four-letter code. Green hues in the topography color palette emphasize the elongate, linear structures forming the Subandean fold-and-thrust belt. Focal mechanisms are for crustal events (<50 km) from the Global Centroid Moment Tensor database with magnitudes that range from M_w 5.2 to 6.6. Yellow circles are epicenters for crustal events from the National Earthquake Information Center. Green circles are a swarm of relocated shallow events (<40 km) including two M_w 4.5–5 earthquakes and associated aftershocks that occurred in October 2013 near the northern MTFS. Also shown for reference is the direction and magnitude of Nazca-South America plate convergence according to NUVEL-1A. AP = Altiplano; EC = Eastern Cordillera; IAZ = Interandean Zone; SSA = southern Subandes; A = The 1998 Aiquile, Bolivia (M_w 6.6), earthquake; cGPS = continuous GPS site; sGPS = roving/campaign GPS site; SCRZ = Santa Cruz; SUCE = Sucre; PTSI = Potosi; CAMR = Camiri; CCDO = Cerro Colorado; COCI = Cocani; COLO = Laguna Colorada; UTUR = Uturuncu; TPZA = Tupiza; TRJA = Tarija; YCBA = Yacuiba; BPSC = Puesto Sucre; Arg. = Argentina; Par. = Paraguay.

with respect to the rupture zone [e.g., *Barbot and Fialko*, 2010; *Hearn*, 2003]. The Subandean GPS network is located hundreds of kilometers northeast of the Tocopilla earthquake epicenter and coseismic slip maxima (Figure 6). Second, the crust and lithospheric mantle structure beneath the central Andes is complex with along- and across-strike variations in crustal thickness, the presence of the strong edge of the Brazilian craton underthrusting the backarc as far west as ~65.5°W, and evidence for lower crust delamination with pockets of high- and low-*P* wave velocity material in the upper mantle [*Beck and Zandt*, 2002] (Figure 9). This complexity lies beneath the GPS network and so likely affects details of the far-field postseismic response. Third, small-scale variations in the poroelastic properties of the Subandean lithosphere could also be a factor. Different crustal rock types exhibit a large range in poroelastic moduli [*Barbot and Fialko*, 2010], and we suspect that variable rheologies are often juxtaposed across large-offset thrusts in the heavily deformed backarc [e.g., *McQuarrie*, 2002].

2.4. Velocity Error Estimation

The presence of time-correlated, colored noise (e.g., flicker, random walk, and power law) in the GPS time series [*Hackl et al*., 2011; *Langbein and Johnson*, 1997; *Mao et al*., 1999; *Williams et al*., 2004; *Zhang et al*., 1997] must be accounted for to create an accurate representation of the regional deformation field. Here we use the est_noise software [*Langbein*, 2004] to compute Gaussian and power law noise statistics (Table S3) and associated velocity uncertainties (Table 1) for the cGPS site time series corrected for Tocopilla earthquake-related deformation and seasonal periodicities. The power law noise model describes many geophysical phenomena [*Agnew*, 1992] and represents an average of the flicker and random-walk noise present in GPS data [*Langbein*, 2012; *Mao et al*., 1999; *Zhang et al*., 1997]. Further, in their comprehensive study of cGPS time series error, *Williams et al*. [2004] report that a power law noise model best describes the data.

For the central Andean backarc cGPS sites we find that when assuming "standard," uncorrelated Gaussian error model, the N, E, and U velocity errors are on average underestimated by factors of 9.0, 8.5, and 5.8, respectively, compared to the white and power law noise model. These factors are on the high end but comparable to previous studies, which show that velocity errors are underestimated by factors ranging from 2 to 11 if a purely white noise model is assumed [*Hackl et al*., 2011; *Mao et al*., 1999; *Williams et al*., 2004; *Zhang et al*., 1997]. For direct comparison, in their analysis of cGPS data from the central Andes, *Kendrick et al*. [1999] find that velocity errors increase by a factor of ~2.5 when they account for temporally correlated noise in their position time series. We suspect that their low scaling factor compared to our analysis is due to the generally poorer quality solutions available at the time resulting in higher daily position scatter (i.e., white noise), which dominated their error budget.

We use a modified version of the method outlined in *Williams* [2003] to compute velocities and associated uncertainties (white and power law noise) for the sGPS sites. We assume that the colored noise present in the GPS data does not vary regionally and form the data covariance matrix using the mean NEU white and power law noise amplitudes. We adopt the maximum NEU power law exponents/indices estimated from the cGPS time series (Table S2) as a conservative measure to account for any residual long-period "noise" introduced during our previous correction steps. We perform a standard least squares inversion using this covariance matrix. Finally, we assume that the a priori noise model is imperfect and scale the formal model covariance by the mean square error of the sGPS time series residuals to obtain a conservative measure of the total velocity uncertainties that reflects the combined white and power law noise. The Gaussian model underestimates the sGPS errors by factors of 6.2, 4.7, and 8.7 for the NEU coordinates, respectively, compared to the white and power law noise model. This reduction in the north and east scale factors when compared to the cGPS scale factors is in agreement with our expectation that standard errors for sGPS sites with long time spans will be closer to the total errors compared to the shorter time span cGPS sites [e.g., *Zhang et al*., 1997]. In other words, standard errors dominate the error budget for sGPS sites. We report the total (white and power law noise) and standard errors (Table 1) and use the total estimates as weighting factors in our velocity field modeling. We also report the uncorrected velocities and associated standard errors in the supporting information (Table S4).

3. New Crustal Velocity Field for the Central Andean Backarc

3.1. Map View Pattern

The corrected backarc velocity field reveals first-order characteristics similar to previous results for the central Andes [e.g., *Bevis et al*., 1999; *Brooks et al*., 2011; *Kendrick et al*., 2001; *Norabuena et al*., 1998]. Vectors are generally oriented subparallel to the ~N78°E Nazca-South America convergence direction [*Angermann et al*., 1999; *Kendrick et al*., 2003] (Figures 1 and 10). In detail, however, the new data reveal a clockwise rotation in the orientation of the vectors from west to east. The mean azimuth of vectors located west of a line of longitude that passes through Tarija (TRJA in Figure 10) is ~N74°E. In contrast, the mean azimuth of Subandean site vectors located between TRJA and the thrust front is ~N89°E. The rotation is most pronounced across the southern, Tarija profile where the mean Subandean velocity vector azimuth is ~N96°E compared to ~N82°E for the northern profile. The rather abrupt change in Tarija profile vector azimuths roughly coincides with the boundary between the Interandean Zone and the SSA (Figure 10).

The velocity vector rotation we observe is consistent with elastic models of oblique plate convergence, which show a decrease in surface velocity obliquity (with respect to the orientation of the trench axis) moving away

from the subduction zone toward the plate interior [*Bevis and Martel*, 2001]. However, despite the notion that the interseismic velocity field reflects elastic, nonpermanent deformation, the observed rotations are also consistent with longer-term, geologic results. *Allmendinger et al*. [2005] show that GPS data from south of the Andean axis of topographic symmetry [*Gephart*, 1994; *Isacks*, 1988] generally exhibit clockwise rotations, which are consistent with those recorded by paleomagnetic and geologic indicators, and suggest that the interseismic velocity field partially reflects long-term, inelastic crustal deformation patterns. Based on late Miocene-Quaternary fold and fault information, early GPS results, and paleomagnetic data, *Lamb* [2000] compute a central Andean horizontal velocity field representative of regional deformation over the last few hundred thousand years. Like we do, they show that vectors in the high Andes are subparallel to the relative plate convergence direction but change to be nearly perpendicular to the range front across the Subandes. Our new velocity field suggests that Subandean structures, which have generally formed from west to east in a foreland-breaking sequence over the past ~10 Myr [e.g., *Echavarria et al*., 2003; *Uba et al*., 2009], may exert a strong control on the modern surface deformation pattern across the SSA. The strike of the Subandean anticlines and synclines changes from north to south and the vectors are by and large oriented orthogonal to these features (Figure 10). This observation is broadly consistent with a model of ductile deformation of the Bolivian lithosphere driven by crustal thickness and topography-induced gravitational stresses [*Lamb*, 2000]. An alternative explanation for the observed Subandean velocity vector rotation specifically may relate to locking on the décollement beneath the fold-and-thrust belt as opposed to far-field affects associated with oblique plate convergence and the subduction zone megathrust [e.g., *Bevis et al*., 2001].

3.2. Velocity Profiles

Horizontal surface velocities gradually decrease away from the Chile trench, and GPS sites located east of the thrust front are essentially not moving with respect to the stable core of the South American craton. Again, this is not dissimilar to previous GPS results for the region, and authors have invoked elastic models of plate boundary locking and the seismic cycle combined with a component of backarc convergence to explain this pattern [e.g., *Bevis et al*., 2001, 1999; *Norabuena et al*., 1998]. Our choice of profile azimuths, perpendicular to the strike of the Subandean ranges, has a modest effect on the projected velocity magnitudes in only the southern profile. The Tarija profile orientation (N100°E) is oblique to the vectors west of TRJA but subparallel to the mean azimuth of the southern profile Subandean site vectors (96°E) resulting in an apparent reduction of the projected velocities for high Andes sites but only a slight change in the profile-parallel SSA velocities. An example of the projection-related reduction in velocities can be seen at the cGPS site UYNI, which has projected northern and southern profile velocities of 15.67 and 13.84 mm/yr, respectively.

The GPS velocity profiles (Figure 11) exhibit features that reflect orogenic wedge processes. These features are not simply a product of our profile azimuth choice and persist if we project the velocities perpendicular to the Chile trench or on to a latitudinal profile. Despite the general eastward decrease in velocities associated with locking of the main plate boundary at the trench, both profiles exhibit a 100–150 km wide zone of roughly constant velocity (that we term a velocity "plateau") with western edges at distances of ~300 km and ~200 km from the thrust front for the northern and southern profiles, respectively. The northern velocity plateau is at ~12 mm/yr, whereas the southern velocity plateau is at ~6 mm/yr and is less well defined due to a group of sites near Entre Rios, Bolivia (ENRI; Figure 11), with projected velocities $\leq$5 mm/yr. For each plateau, the western edge of the constant velocity region roughly coincides with the Eastern Cordillera (EC)/Interandean Zone (IAZ) boundary (Figure 11). This coincidence is significant because the EC is generally viewed as the backstop or bulldozer [e.g., *Davis et al*., 1983] driving SSA deformation since ~10 Ma [*Allmendinger et al*., 1983; *Gubbels et al*., 1993; *Kley*, 1996]. Thus, the ~100–150 km wide, constant velocity plateaus apparent in the new GPS-derived velocity field delineate both the back of the wedge, including the inactive (IAZ) and active (SSA) portions, and the approximate slip rate or wedge loading rate on the basal décollement.

East of the velocity plateaus, both profiles both exhibit sharp velocity decreases before reaching ~0 mm/yr adjacent to the thrust front. The distances over which the reductions in velocity occur are ~100 km and ~50 km for the northern and southern profiles, respectively. We refer to these decreases as the northern and southern east flank velocity gradients and note that the velocities decrease to ~0 mm/yr ~30–40 km west of the thrust front (Figure 11). Again, as with the velocity plateaus, the northern east flank velocity gradient is prominent and clearly defined by approximately nine sites west of CAMR, whereas the southern east flank

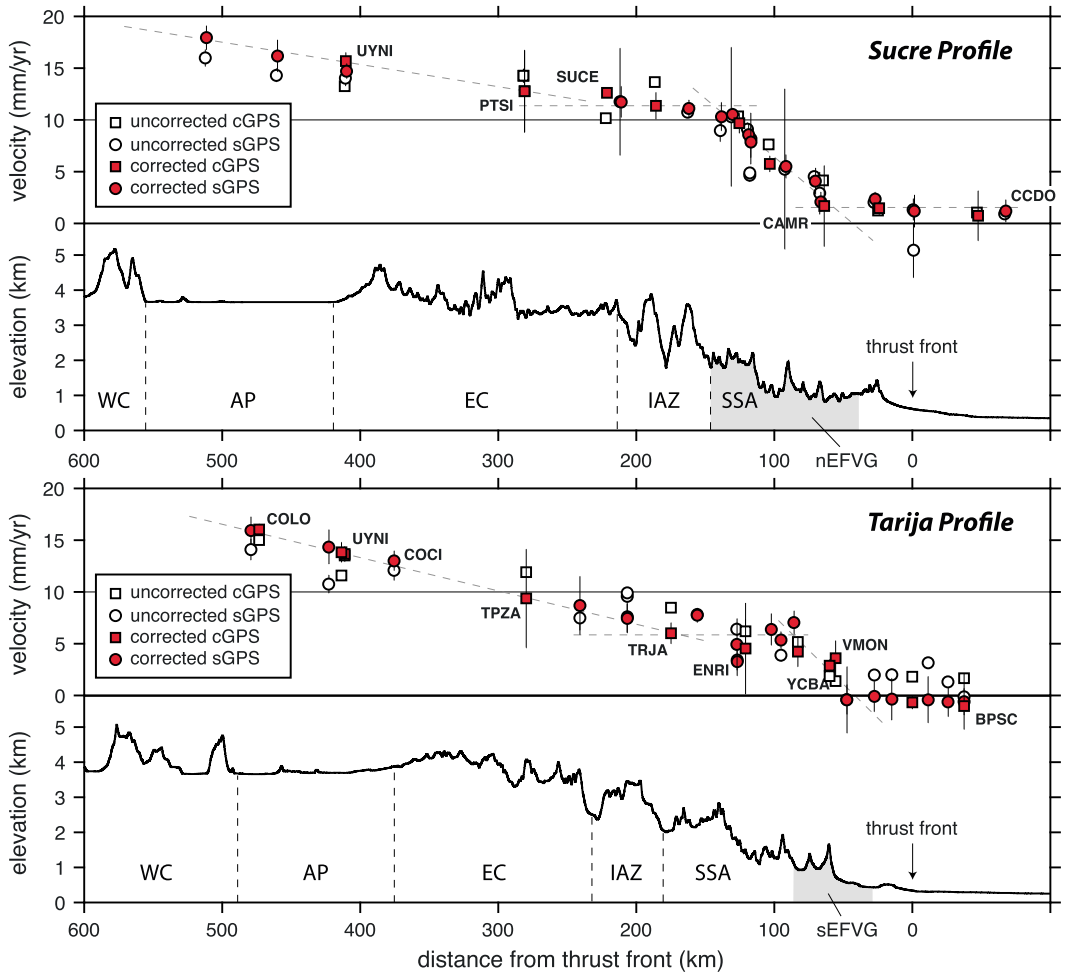

Figure 11. Profile views of the new surface velocity field projected perpendicular to the (first and second panels) strike of the Subandean structures with corrected 2 sigma error bars and the (third and fourth panels) corresponding topography. See Figure 1 for profile locations. White symbols are uncorrected velocities and errors (Table S4), and red symbols are earthquake transient corrected velocities and errors. Light dashed lines are hand-drawn fits to the data intended to emphasize the features referred to in the text. The approximate locations of the physiographic boundaries are indicated with vertical dashed lines beneath the topography. The gray shaded region under the topography corresponds to the east flank velocity gradients. Labeled GPS sites are the same as in Figure 9. WC = Western Cordillera; AP = Altiplano; EC = Eastern Cordillera; IAZ = Interandean Zone; SSA = southern Subandes; nEFVG/sEFVG = northern/southern east flank velocity gradient; VMON = Villamontes; ENRI = Entre Rios.

velocity gradient is far less distinct due to its narrow width and the lack of GPS sites immediately adjacent to VMON and YCBA (Figure 11).

The location of the east flank velocity gradients with respect to the Subandean structures also varies along strike. The western limit of the wide, northern east flank velocity gradient corresponds to the IAZ/SSA boundary and its eastern edge is located near the range front (as opposed to thrust front) Charagua anticline (Figures 10 and 11). In contrast, the narrow southern east flank velocity gradient lies exclusively within the front of the active wedge encompassing only the first couple of range-front thrusts.

3.3. Backarc Velocity Field Modeling

To investigate strain accumulation across the Subandean orogenic wedge, we model the eastern portion of the corrected GPS velocity field, including the constant velocity plateaus described above, using rectangular dislocations in an elastic half-space [*Okada*, 1985]. This approach is commonly used to investigate interseismic stress and strain accumulation at subduction zones and is also valid for modeling surface displacements associated with large intracontinental thrust faults including the décollements of active orogenic wedges

[*Bilham et al*., 1997; *Brooks et al*., 2011; *Hsu et al*., 2003; *Vergne et al*., 2001]. We exclude velocities for sites located west of the velocity plateaus as locking of the main plate boundary at the Chile trench has been examined in detail by others [e.g., *Bevis et al*., 2001; *Chlieh et al*., 2011; *Kendrick et al*., 2006; *Norabuena et al*., 1998].

Brooks et al. [2011] stacked central Andean backarc surface velocities onto a single Chile trench-perpendicular profile. Here we model the northern and southern sites separately as our denser, more precise data set provides an opportunity to investigate along-strike variations in the décollement properties. The strike of the Subandean structures changes from north to south, so we project the northern and southern data on to ENE and ESE oriented profiles, respectively, to view and model the sites in a structure-perpendicular reference frames (Figure 10). For example, although separated in map view by ~85 km, the cGPS sites VMON and YCBA are located on the eastern flank of the Aguarague anticline (Figure 11). Only if we project the Tarija profile sites on to an azimuth oriented approximately perpendicular to the strike of this structure do they plot adjacent to one another.

We simulate continuous, uniform slip on the gently dipping décollement at the base of the wedge using the seismic cycle or back-slip model of strain accumulation and release at a subduction zone [*Savage*, 1983]. In this model strain accumulation is attributed to steady aseismic slip at depth on the basal fault towards the mountain interior, while the shallow, updip portion of the fault remains locked. By superposing elastic dislocation solutions for a steady state, reverse fault with stable sliding along its entire length and a shallow back-slip fault with equal yet opposite motion (normal slip), we impose a no-slip condition on the up-dip portion of the dislocation that represents the locked portion. As a result, the maximum gradient in the horizontal velocity field overlies the slipping-to-locked transition [*Bilham et al*., 1998; *Okada*, 1985; *Savage*, 1983].

We assume a standard Poisson's ratio of 0.25 [*Brooks et al*., 2011; *Vergne et al*., 2001] and compare the dislocation model and GPS surface velocities and explore the multidimensional parameter space using a grid search inversion approach [e.g., *Weiss et al*., 2015]. We compare all three components of the velocity field (NEU) to the model noting that inclusion of the vertical velocities helps constrain the depth to the slipping-to-locked transition in particular. We reduce the typical nine parameter (dislocation upper left corner *x*,*y*, and *z* position; dislocation length, width, depth, strike, and dip; magnitude of strike-slip and dip-slip) problem to five by making the following simplifying assumptions: the dislocation is very long (across-strike) and wide (along-strike), resulting in modeled deformation that is essentially plane strain, each profile is oriented perpendicular to the strike of the underlying dislocation, the updip limit of the dislocation is located directly beneath the easternmost emergent thrust front structures, and there is no opening mode component of displacement across the dislocation. These assumptions leave us with five dislocation parameters for our grid search including (1) dip, (2) strike slip, (3) dip slip, (4) downdip width of the locked zone (W_L), and (5) depth to slipping-to-locked transition. We define unique dislocation geometries by varying each of these parameters and computing the weighted sum of squares misfit between the model and data where the data are the corrected NEU velocities and the weighting factors are the corresponding standard deviations (Table 1). We present our results in the form of probability distributions of the dislocation parameters by following the approach of *Weiss et al*. [2015] and converting the misfit to probabilities using the joint probability density function [*Menke*, 1989] (Figure 12). Although we refrain from placing any a priori constraints on the model parameters for our grid search, we note that balanced cross sections from the region indicate that the Subandean décollement is subhorizontal with a dip of ~2° at a depth of 10 ± 5 km beneath the surface [*Baby et al*., 1997; *Dunn et al*., 1995; *Giraudo and Limachi*, 2001; *McQuarrie*, 2002].

The dislocation parameter distributions for the profiles reveal different behavior for portions of the wedge located ~200 km apart. In the north, the model indicates that the décollement is subhorizontal, dipping gently to the west (<5°) and slipping at rates of ~14 mm/yr (*U*2; dip-slip) and ~1 mm/yr (*U*1 sinistral; left-lateral strike-slip). The width of the locked zone (W_L) is ~100 km, and the depth to the slipping-to-locked transition is ~13 km. The reported peak parameter distribution values all fall within the 95% confidence regions of the *Brooks et al*. [2011] results and are consistent with some structural and geophysical observations (Figure 12). For example, the model dislocation dip and depth are within the values suggested by regional cross sections. The slipping-to-locked transition from the best model, which we define as the peaks (modes) of the corresponding probability distributions, intersects both the basal décollement from published cross sections [*Dunn et al*., 1995; *Giraudo and Limachi*, 2001] and the 300°C isotherm calculated from the backarc

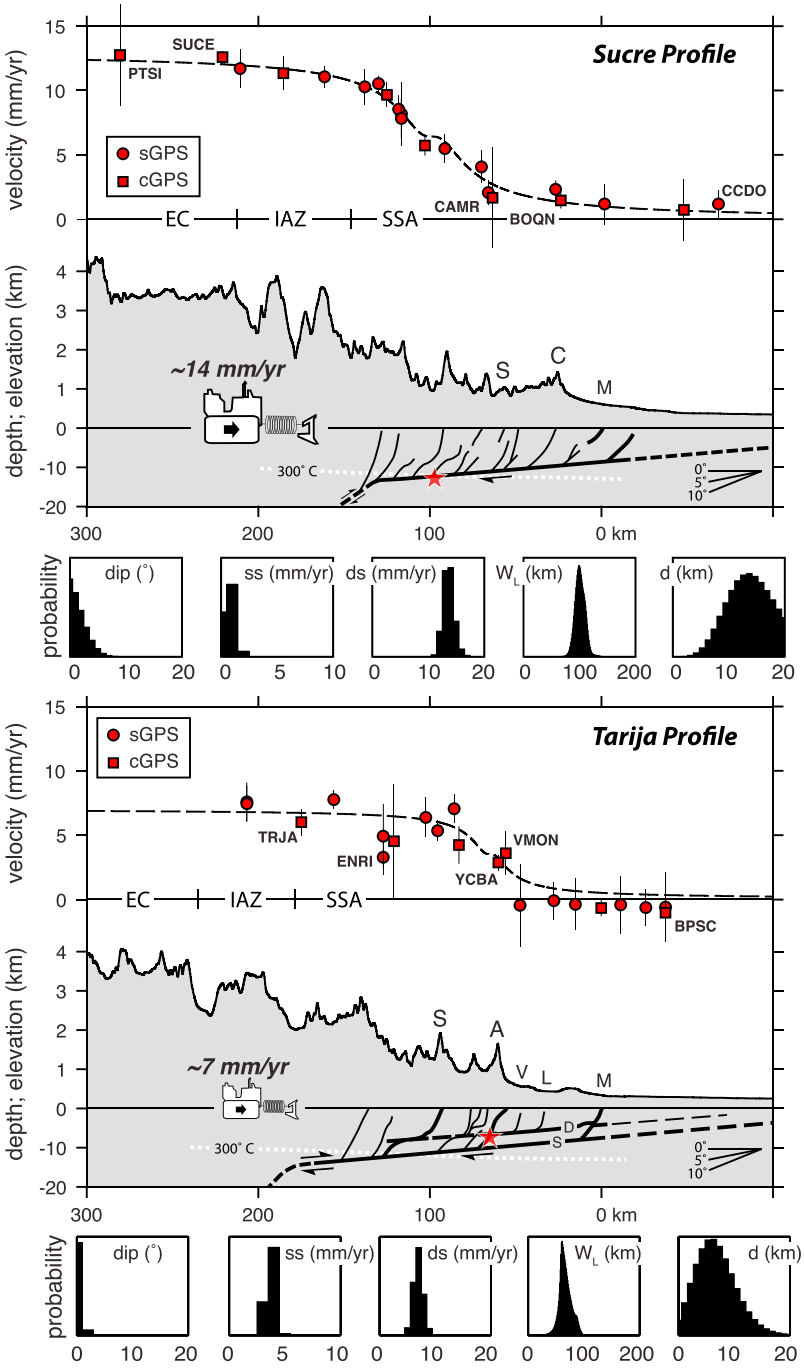

Figure 12. Subandean orogenic wedge elastic dislocation modeling results. (top) The projected velocities and corrected 2 sigma error bars for the active wedge portion of the velocity field only. The black dashed line is the best model from the grid search inversion. Select GPS sites are labeled with their four-letter station codes. (bottom) The topography extracted from the profiles with faults from published cross sections. Profile locations are shown in Figure 1. The northern, Sucre profile, and southern, Tarija profile, geologic cross sections are profiles D and B from *Giraudo and Limachi* [2001]. The approximate boundaries between the major physiographic provinces are labeled. The star in the subsurface indicates the slipping-to-locked transition from the best model and the white dashed line is the 300°C isotherm calculated from the central Andean backarc geothermal gradient [*Currie and Hyndman*, 2006]. Also shown are the probability distributions for each of the model parameters with the peaks correspond to the aforementioned best model values. Spring-loaded bulldozers are labeled with the wedge loading rate from the peak of the dip-slip probability distributions. ENRI = Entre Rios; BOQN = Los Boquerones (Charagua); S = Suaruro structure; C = Charagua structure; A = Aguarague structure; V = Villamontes structure; L = La Vertiente structure; M = Mandeyapecua fault; D = detachment surface in Devonian Los Monos shale; S = main detachment in the Silurian Kirusillas Formation; ss = strike-slip; ds = dip-slip; W_L = locked width; d = depth.

geothermal gradient [*Currie and Hyndman*, 2006]. The latter intersection is particularly significant as 300°C indicates the approximate transition from velocity-strengthening (continuous creep) to velocity weakening (stick-slip) behavior in quartzo-feldspathic rocks, which is where earthquakes will tend to nucleate [*Scholz*, 1988, 1998]. The probability distribution peak for the dip-slip parameter of 14 mm/yr, which we equate to the loading rate at the back of the orogenic wedge, also compares favorably with the SSA Plio-Quaternary shortening rate estimates of 7–13 mm/yr [*Mugnier et al*., 2006, and references therein] and is slightly faster than the *Brooks et al*. [2011] best model value of 11.1 mm/yr.

The southern profile model results indicate that the décollement is also subhorizontal, dipping gently to the west (<5°), while slipping at rates of ~7 mm/yr (*U*2; dip slip), which is within the range of Plio-Quaternary shortening estimates but one half of the northern rate, and ~4 mm/yr (*U*1 sinistral; left-lateral strike-slip). The southern W_L of ~61 km is significantly less than the northern W_L, and the slipping-to-locked transition depth of ~7 km falls within the 10 ± 5 km range constrained by balanced cross sections from the region [e.g., *Allmendinger and Zapata*, 2000].

4. Discussion of Modeling Results

Although we have already drawn comparisons between geologic observations and our new GPS velocity field and modeling results, a few additional points are worth mentioning. Apart from some minor differences in W_L and the dip-slip rate, our northern profile results are nearly identical to *Brooks et al*. [2011] and suggest that rupture nucleates somewhere between the slipping-to-locked transition and the thrust front and may propagate updip toward the thrust front resulting in shallow fault-related folding and/or surface rupture [*Brooks et al*., 2011; *Weiss et al*., 2015]. The well-defined, smooth northern east flank velocity gradient pattern is indicative of locking on the basal décollement and not motion of individual surface faults or fault blocks [e.g., *Lamb and Smith*, 2013].

The Tarija profile results are less straightforward suggesting that a more detailed modeling approach may be required to match some of the geologic information. We suspect that the southern subsurface complexity, which is readily apparent when comparing the two geologic cross sections (Figure 12), may be influencing the GPS results. In the vicinity of the Tarija profile, in addition to the primary detachment surface located at the base of the Silurian Kirusillas Formation, a shallower, secondary décollement exists within the Devonian Los Monos shale (Figure 11). The faults that generated both the Villamontes and La Vertiente structures cut up from the shallow detachment, which also links the large Aguarague surface fold and additional wedge-interior faults, including the Suaruro structure, to the deeper, primary detachment [*Dunn et al*., 1995; *Giraudo and Limachi*, 2001; *Uba et al*., 2009]. The location of the southern slipping-to-locked transition, to the east of the presumed active Aguarague and Suaruro thrusts [*Lamb*, 2000; *Mugnier et al*., 2006], and closer to the shallower décollement, combined with the fact that simultaneous activity of both detachments is actually required to restore the geologic cross section in the vicinity of the southern profile [*Dunn et al*., 1995], probably indicates that both are active. This suggestion, however, contrasts the recent findings of *Rocha and Cristallini* [2015] who infer significant involvement of the shallower Los Monos detachment in the north only.

We suggest that the complex southern velocity plateau may be a manifestation of a number of factors including the presence of active thrust ramps, the relative motions of individual fault blocks above the creeping portion of the system, and evidence for multiple active décollements. We find it interesting that the mean shortening rate estimate for the Aguarague structure from the fluvial incision study of *Mugnier et al*. [2006], which lies above our estimated slipping-to-locked transition, is identical to the southern wedge loading rate of 7 mm/yr. It may be that the stream incision-based rate is a reflection of the continuously slipping portion of the system located to the west of the Aguarague structure.

Figure 13 compares our new, GPS-based wedge loading rates with whole-wedge, wedge-front fault system, and fluvial incision-based shortening rate estimates. Published geologic cross sections for the SSA indicate the long-term (Myr) shortening rate is ~7–13 mm/yr [*Baby et al*., 1997; *Dunn et al*., 1995; *Gubbels et al*., 1993; *Leturmy et al*., 2000; *McQuarrie*, 2002; *McQuarrie et al*., 2005; *Uba et al*., 2006]. In general, this range of rates closely matches our GPS-based results of 14 and 7 mm/yr for the northern and southern profiles, respectively; the Sucre and Tarija profile wedge loading rates overlap the upper and lower limits of the range in estimated geologic shortening (Figure 13). The suggested north-to-south reduction in the amount of total Subandean shortening moving away from the axis of the prominent bend in the Andean mountain belt

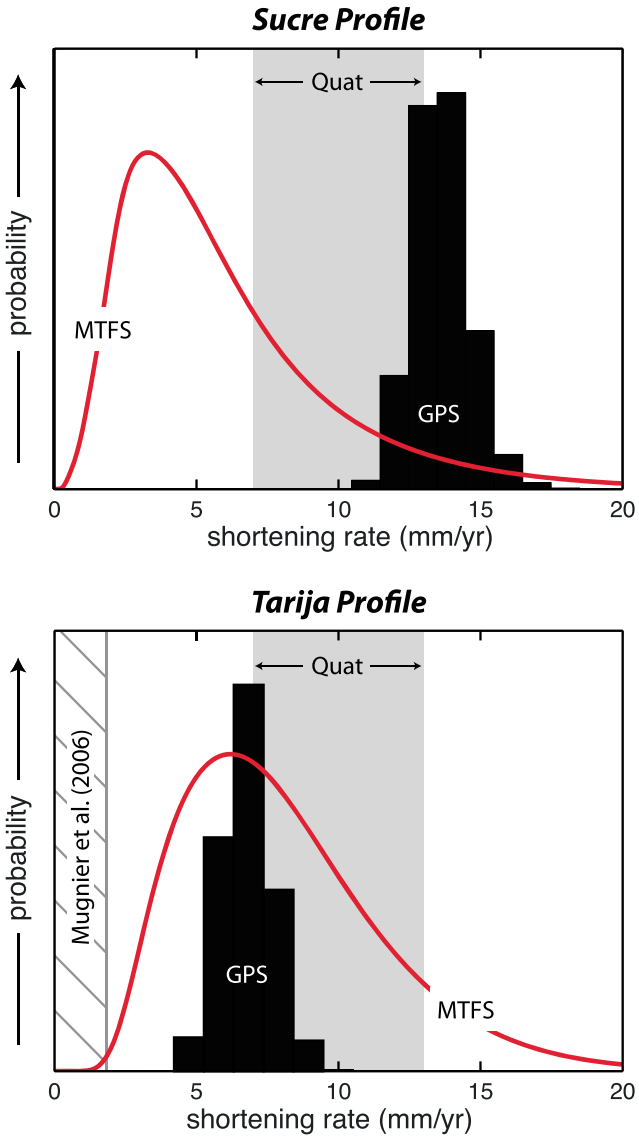

Figure 13. A comparison of shortening rate estimates over multiple timescales for the Sucre and Tarija profiles. The gray bars indicate the range in whole-wedge Quaternary shortening rates of 7–13 mm/yr estimated from geologic cross sections. The black histograms are the dislocation-based modeling results of the new backarc surface velocity field (Figure 11). The red curves are Quaternary shortening rate probability density functions (pdf) for the wedge-front Mandeyapecua thrust fault system (Figure 9) based on the analysis presented in *Weiss et al.* [2015]. The pdfs were computed by summing the dip-slip rate pdfs from the profiles shown in Figure 8 of *Weiss et al.* [2015] Profiles 1–5 were summed to create the Sucre profile pdf and profiles 7–8 were summed to create the Tarija profile pdf. The minimum Mandeyapecua fault slip rate pdfs were used in both [see *Weiss et al.*, 2015, Figures 7 and 8], and dip-slip rate pdfs from *Weiss et al.* [2015] were converted to shortening rate pdfs using the corresponding fault dip angle distributions [*Weiss et al.*, 2015]. The hatched region in the Tarija profile comparison indicates the estimated 1 ± 1 mm/yr Holocene shortening rate for the Mandeyapecua (Iguitini) fault from the stream incision analysis of *Mugnier et al.* [2006].

(~150 km near Santa Cruz to ~70 km near the Argentinean border over the ~10 Myr duration of Subandean shortening) [*Lamb*, 2000] is also consistent with our new GPS-based results.

However, a marked north-to-south shortening rate discrepancy is apparent when we consider the wedge-front Mandeyapecua thrust fault system (MTFS) [*Weiss et al.*, 2015]. In the south, the various shortening rate estimates, which encompass geologic, neotectonic, and geodetic timescales, show a close agreement (Figure 13). More specifically, the MTFS shortening rate for the Tarija profile overlaps both the GPS and whole-wedge rates suggesting that the slip rate at the back of the wedge is accommodated solely by the wedge-front fault system and that this has been the case for the last ~2–3 Myr. On the other hand, evidence for active faulting associated with structures other than those at the wedge front in the vicinity of the Tarija profile, and specifically the Aguarague and Suaruro thrusts (Figure 12) [*Lamb*, 2000; *Mugnier et al.*, 2006], seems to be at odds with this result. The apparent discrepancy may reflect the stochastic or chaotic nature of rupture propagation seen in some recent numerical models of wedge deformation [*Mary et al.*, 2013a; *Yagupsky et al.*, 2014], which indicate that faulting can potentially occur spontaneously at any location in the wedge. Our results show that the bulk of the slip reaches the wedge-front fault system in the south but do not rule out the possibility of some component of internal wedge deformation as well.

Alternatively, the evidence for internal wedge deformation may indicate that the southern SSA has recently transitioned to a different phase of the underthrusting-accretion (i.e., thickening-widening) wedge growth cycle [*Del Castello and Cooke*, 2007]. Analogue and numerical models have shown that wedges evolve via distinct phases of widening, when new thrusts nucleate at the front of the wedge, and

thickening via internal (out-of-sequence) deformation on existing structures [*Adam et al*., 2005; *Del Castello and Cooke*, 2007; *Hoth et al*., 2007; *Yagupsky et al*., 2014].

The geodetic signal associated with this cycle has yet to be documented, but a few lines of evidence point towards a possible correspondence in the SSA. *Mugnier et al*. [2006] calculate shortening rates of 1 ± 1, 7 ± 3.5, and 2.5 ± 1.5 mm/yr for the Mandeyapecua, Aguarague, and Suaruro faults, respectively (Figures 12 and 13). These rates, which are based on a geomorphic analysis of the southern Subandean-crossing Rio Pilcomayo and presumably represent an average over the Holocene period, suggest that most of the recent deformation is absorbed by internal structures and not by the MTFS, which has accommodated most of the Quaternary shortening [*Weiss et al*., 2015] (Figure 13). This cyclicity may be the rule rather than the exception across the southern SSA; *Uba et al*. [2009] present evidence for an older cycle of wedge widening/thickening in the vicinity of the Tarija profile when the deformation front propagated from the western Subandes to the La Vertiente structure (V in Figure 12) between 12 and 6 Ma (widening), subsequently retreated to internal locations (thickening) and advanced to the modern thrust front from 4 to 2 Ma (widening). Taken in the context of these observations, our results point towards the possibility of a rejuvenated phase of underthrusting in the vicinity of the Tarija profile.

The peak of the northern MTFS shortening rate estimate that probability distribution lies well beneath the 7–13 mm/yr whole-wedge and the geodetically determined ~14 mm/yr shortening rates, indicating that a slip deficit of at least ~50% may characterize the wedge front near the Sucre profile (Figure 13). This also happens to be the youngest part of the MTFS [*Weiss et al*., 2015]. We are unaware of any neotectonic studies across the northern SSA, so we cannot directly attribute the deficit to internal wedge deformation or draw such direct comparisons over multiple timescales like we can in the south. Despite few modern and historical earthquakes, there is some distributed crustal seismicity including strike-slip events north of Sucre, a few scattered shallow thrust-related events across the northern SSA and IAZ, and a notable recent cluster of M_w 4.5–5 earthquakes and associated aftershocks across the northern MTFS (Figure 10). Based on the aforementioned combination of observations, including modeling results that reveal a simpler picture of strain accumulation and release in slip events that bypass internal structures and rupture faults at the wedge tip, we suggest that the wedge in the vicinity of the Sucre profile is either in or transitioning to a frontal accretion and widening phase. This suggestion is in line with a recent wedge stress state analysis, which posits that in general megathrust décollement rupture will preferentially propagate to the wedge toe rather than break upward along preexisting, internal structures [*Hubbard et al*., 2015].

An alternative explanation for the Sucre profile deficit relates to the correspondence between narrower wedge width, steeper wedge taper angle, and elevated rates of precipitation-induced erosion that characterize the northern SSA [*Barnes et al*., 2012; *Horton*, 1999; *Masek et al*., 1994; *McQuarrie et al*., 2008; *Whipple*, 2009]. Numerical, analytical, and analogue models all tend to predict a decrease in mountain width and distributed internal wedge deformation in response to a climate-driven increase in erosion rates [e.g., *Cruz et al*., 2010; *Hilley and Strecker*, 2004; *Mary et al*., 2013b; *Whipple and Meade*, 2004]. If the observed MTFS shortening rate deficit is a persistent feature, it could point towards long-lived, albeit currently undetected, internal wedge deformation in response to external, climatic forcing. A stream incision analysis of the central range-crossing Rio Parapeti and/or the northern Rio Grande similar to the Rio Pilcomayo investigation in the south [*Mugnier et al*., 2006] would be one way to address this possibility by quantifying recent internal wedge deformation.

5. Conclusions

We present a new surface velocity field for the central Andean backarc based on data from survey and continuous GPS sites across the Altiplano, Eastern Cordillera, Interandean Zone, southern Subandes, and adjacent foreland. Despite the notion that the backarc is isolated from the subduction zone earthquake cycle, we find that earthquakes at the Chile trench, and specifically both the 2007 M_w 7.7 Tocopilla and 2014 M_w 8.2 Pisagua events, perturb the GPS time series. The backarc velocity field, corrected for seasonal and earthquake affects, reveals that surface velocities gradually decrease away from the Chile trench and sites are essentially stable east of the thrust front. Vectors rotate and are perpendicular to the strike of the topography across the fold-and-thrust belt, lending support to the [*Lamb*, 2000] hypothesis that topography-induced stresses may be a driver of surface deformation. Profile views of the new velocity field reveal distinct regions that reflect (1) locking of the main plate boundary across the high Andes, (2) the location of and loading rate at

the back of the orogenic wedge, and (3) an east flank velocity gradient indicative of décollement locking beneath the Subandes. We document a substantial north to south decrease in the wedge loading rate (14 versus 7 mm/yr), décollement locked width (100 versus 61 km), and the décollement slipping-to-locked transition depth (13 versus 7 km) but neither the data or correspondence between the model and the geology is as clear in the south, and we suggest this may reflect simultaneous activity of multiple detachments and/or motion of internal wedge fault blocks. A comparison of the new GPS modeling results with shortening rates estimated over a range of timescales suggests the northern and southern SSA may be in different phases of the underthrusting-accretion cycle [e.g., *Del Castello and Cooke*, 2007]; the southern wedge appears to have recently transitioned to a thickening phase via internal deformation along preexisting faults (underthrusting), whereas the northern wedge is in a widening phase characterized by faulting at the wedge toe (accretion). With respect to regional seismic hazard, although earthquakes may nucleate anywhere between the slipping-to-locked transition, our results suggest that coseismic surface rupture and/or subsurface folding is most likely to occur in association with the thrust front fault system in the north, whereas rupture of internal wedge thrust faults may occur in the south and the wedge front.

Acknowledgments

This study was supported by the National Science Foundation (grants EAR-1443317 and EAR-1118481). We thank Jeanne Hardebeck of the USGS for providing relocated Bolivian thrust front earthquake information. We thank our collaborators at the Instituto Geográfico Militar de Bolivia and the Centro de Procesamiento y Analysis GNSS including Angel Mollericona, Hilario Cruz, Ricardo Carita, Marcelo Segales, Nelson Olivera, Tito Flores, Daniel Espinoza, Wilson Soria, Wilber Delgado, David Morales, Ricardo Carita, Jose Marquez, Jorge Arteaga, and Moises Lopez. The local knowledge, experience, and expertise of Roger Tinta Sallico in particular proved to be indispensable on countless occasions. We also thank Andrew Barbour and Eileen Evans of the USGS and Garrett Ito of the University of Hawaii for their careful reading and suggestions that significantly improved the manuscript. The paper also benefits greatly from the reviews of Editor André Revil, Ernesto Cristallini, and an anonymous reviewer. The Generic Mapping Tools software [*Wessel et al*., 2009] was used to prepare Figures 1–4, 6, 9–12, S1, and S3. The data for this paper are available by contacting Jonathan R. Weiss at jweiss@hawaii.edu or James H. Foster at jfoster@soest.hawaii.edu. This is SOEST contribution 9709.

References

Adam, J., J. L. Urai, B. Wieneke, O. Oncken, K. Pfeiffer, N. Kukowski, J. Lohrmann, S. Hoth, W. van der Zee, and J. Schmatz (2005), Shear localisation and strain distribution during tectonic faulting—New insights from granular-flow experiments and high-resolution optical image correlation techniques, *J. Struct. Geol.*, *27*(2), 283–301, doi:10.1016/j.jsg.2004.08.008.

Agnew, D. C. (1992), The time-domain behavior of power-law noises, *Geophys. Res. Lett.*, *19*(4), 333–336, doi:10.1029/91GL02832.

Allmendinger, R. W., V. A. Ramos, T. E. Jordan, M. Palma, and B. L. Isacks (1983), Paleogeography and Andean structural geometry, northwest Argentina, *Tectonics*, *2*(1), 1–16, doi:10.1029/TC002i001p00001.

Allmendinger, R. W., R. Smalley Jr., M. Bevis, H. Caprio, and B. A. Brooks (2005), Bending the Bolivian orocline in real time, *Geology*, *33*(11), 905–908.

Allmendinger, R. W., and T. R. Zapata (2000), The footwall ramp of the Subandean decollement, northernmost Argentina, from extended correlation of seismic reflection data, *Tectonophysics*, *321*, 37–55.

Angermann, D., J. Klotz, and C. Reigber (1999), Space-geodetic estimation of the Nazca-South America Euler vector, *Earth Planet. Sci. Lett.*, *171*(3), 329–334.

Avouac, J.-P., L. Meng, S. Wei, T. Wang, and J.-P. Ampuero (2015), Lower edge of locked Main Himalayan Thrust unzipped by the 2015 Gorkha earthquake, *Nat. Geosci.*, *8*(9), 708–711, doi:10.1038/ngeo2518.

Baby, P., P. Rochat, G. Mascle, and G. Herail (1997), Neogene shortening contribution to crustal thickening in the backarc of the central Andes, *Geology*, *25*(10), 883–886.

Barbot, S., and Y. Fialko (2010), A unified continuum representation of post-seismic relaxation mechanisms: Semi-analytic models of afterslip, poroelastic rebound and viscoelastic flow, *Geophys. J. Int.*, *182*(3), 1124–1140, doi:10.1111/j.1365-246X.2010.04678.x.

Barnes, J. B., T. A. Ehlers, N. Insel, N. McQuarrie, and C. J. Poulsen (2012), Linking orography, climate, and exhumation across the central Andes, *Geology*, *40*(12), 1135–1138.

Beck, S. L., and G. Zandt (2002), The nature of orogenic crust in the central Andes, *J. Geophys. Res.*, *107*(B10), 16, doi:10.1029/2000JB000124.

Bejar-Pizarro, M., et al. (2010), Asperities and barriers on the seismogenic zone in North Chile: State-of-the-art after the 2007 M_w 7.7 Tocopilla earthquake inferred by GPS and InSAR data, *Geophys. J. Int.*, *183*(1), 390–406, doi:10.1111/j.1365-246X.2010.04748.x.

Bevis, M., D. Alsdorf, E. Kendrick, L. P. Fortes, B. Forsberg, R. S. J. Smalley, and J. Becker (2005), Seasonal fluctuations in the mass of the Amazon River system and Earth's elastic response, *Geophys. Res. Lett.*, *32*, L16308, doi:10.1029/2005GL023491.

Bevis, M., Y. Bock, P. Fang, R. Reilinger, T. Herring, J. Stowell, and R. J. Smalley (1997), Blending old and new approaches to regional geodesy, *Eos Trans. AGU*, *78*(6), 61–66, doi:10.1029/97EO00040.

Bevis, M., and A. Brown (2014), Trajectory models and reference frames for crustal motion geodesy, *J. Geod.*, *88*(3), 283–311, doi:10.1007/s00190-013-0685-5.

Bevis, M., E. Kendrick, R. J. Smalley, B. A. Brooks, R. Allmendinger, and B. Isacks (2001), On the strength of interplate coupling and the rate of backarc convergence in the central Andes: An analysis of the interseismic velocity field, *Geochem. Geophys. Geosyst.*, (*2*), 1067, doi:10.1029/2001GC000198.

Bevis, M., E. C. Kendrick, R. Smalley Jr., T. Herring, J. Godoy, and F. Galban (1999), Crustal motion north and south of the Arica deflection: Comparing recent geodetic results from the central Andes, *Geochem. Geophys. Geosyst.*, *1*, 1005, doi:10.1029/1999GC000011.

Bevis, M., and S. Martel (2001), Oblique plate convergence and interseismic strain accumulation, *Geochem. Geophys. Geosyst.*, *2*, 1003 doi:10.1029/2000GC000125.

Bilham, R., F. Blume, R. Bendick, and V. K. Gaur (1998), Geodetic constraints on the translation and deformation of India: Implications for future great Himalayan earthquakes, *Curr. Sci.*, *74*(3), 213–229.

Bilham, R., et al. (1997), GPS measurements of present-day convergence across the Nepal Himalaya, *Nature*, *386*(6620), 61–64.

Blewitt, G., and D. Lavallée (2002), Effect of annual signals on geodetic velocity, *J. Geophys. Res.*, *107*(B7), ETG 9-1–ETG 9-11, doi:10.1029/2001JB000570.

Bollinger, L., S. N. Sapkota, P. Tapponnier, Y. Klinger, M. Rizza, J. Van der Woerd, D. R. Tiwari, R. Pandey, A. Bitri, and S. Bes de Berc (2014), Estimating the return times of great Himalayan earthquakes in eastern Nepal: Evidence from the Patu and Bardibas strands of the Main Frontal Thrust, *J. Geophys. Res. Solid Earth*, *119*, 7123–7163, doi:10.1002/2014JB010970.

Brooks, B. A., M. Bevis, R. J. Smalley, E. Kendrick, R. Manceda, E. Lauria, R. Maturana, and M. Araujo (2003), Crustal motion in the Southern Andes (26°–36°S): Do the Andes behave like a microplate?, *Geochem. Geophys. Geosyst.*, *4*(10), 1085, doi:10.1029/2003GC000505.

Brooks, B. A., et al. (2011), Orogenic-wedge deformation and potential for great earthquakes in the central Andean backarc, *Nat. Geosci.*, *4*(6), 380–383, doi:10.1038/Ngeo1143.

Bürgmann, R., P. A. Rosen, and E. J. Fielding (2000), Synthetic aperture radar interferometry to measure Earth's surface topography and its deformation, *Annu. Rev. Earth Planet. Sci.*, *28*(1), 169–209, doi:10.1146/annurev.earth.28.1.169.

Chlieh, M., H. Perfettini, H. Tavera, J. P. Avouac, D. Remy, J. M. Nocquet, F. Rolandone, F. Bondoux, G. Gabalda, and S. Bonvalot (2011), Interseismic coupling and seismic potential along the central Andes subduction zone, *J. Geophys. Res.*, *116*, B12405, doi:10.1029/2010JB008166.

Cruz, L., J. Malinski, A. Wilson, W. A. Take, and G. Hilley (2010), Erosional control of the kinematics and geometry of fold-and-thrust belts imaged in a physical and numerical sandbox, *J. Geophys. Res.*, *115*, B09404, doi:10.1029/2010JB007472.

Currie, C. A., and R. D. Hyndman (2006), The thermal structure of subduction zone backarcs, *J. Geophys. Res.*, *111*, B08404, doi:10.1029/2005JB004024.

Dahlen, F. A., J. Suppe, and D. Davis (1984), Mechanics of fold-and-thrust belts and accretionary wedges-cohesive Coulomb theory, *J. Geophys. Res.*, *89*(NB12), 87–101, doi:10.1029/JB089iB12p10087.

Davis, D., J. Suppe, and F. A. Dahlen (1983), Mechanics of fold-and-thrust belts and accretionary wedges, *J. Geophys. Res.*, *88*(NB2), 1153–1172, doi:10.1029/JB088iB02p01153.

DeDontney, N., J. R. Rice, and R. Dmowska (2012), Finite element modeling of branched ruptures including off-fault plasticity, *Bull. Seismol. Soc. Am.*, *102*(2), 541–562, doi:10.1785/0120110134.

Del Castello, M., and M. L. Cooke (2007), Underthrusting-accretion cycle: Work budget as revealed by the boundary element method, *J. Geophys. Res.*, *112*, B12404, doi:10.1029/2007JB004997.

Delouis, B., M. Pardo, D. Legrand, and T. Monfret (2009), The M_w 7.7 Tocopilla earthquake of 14 November 2007 at the southern edge of the Northern Chile seismic gap: Rupture in the deep part of the coupled plate interface, *Bull. Seismol. Soc. Am.*, *99*(1), 87–94, doi:10.1785/0120080192.

Dunn, J. F., K. G. Hartshorn, and P. W. Hartshorn (1995), Structural styles and hydrocarbon potential of the sub-Andean thrust belt of Southern Bolivia, in *Petroleum Basins of South America*, edited by A. J. Tankard, R. Suarez Soruco, and H. J. Welsink, pp. 523–543.

Echavarria, L., R. Hernandez, R. Allmendinger, and J. Reynolds (2003), Subandean thrust and fold belt of northwestern Argentina: Geometry and timing of the Andean evolution, *AAPG Bull.*, *87*(6), 965–985.

Elliott, J. R., R. Jolivet, P. J. Gonzalez, J. P. Avouac, J. Hollingsworth, M. P. Searle, and V. L. Stevens (2016), Himalayan megathrust geometry and relation to topography revealed by the Gorkha earthquake, *Nature Geosci.*, *9*(2), 174–180, doi:10.1038/ngeo2623.

England, P., and J. Jackson (1989), Active deformation of the continents, *Annu. Rev. Earth Planet. Sci.*, *17*(1), 197–226, doi:10.1146/annurev.ea.17.050189.001213.

England, P., and J. Jackson (2011), Uncharted seismic risk, *Nat. Geosci.*, *4*(6), 348–349, doi:10.1038/ngeo1168.

England, P., and D. McKenzie (1982), A thin viscous sheet model for continental deformation, *Geophys. J. R. Astron. Soc.*, *70*(2), 295–321, doi:10.1111/j.1365-246X.1982.tb04969.x.

England, P., and P. Molnar (1997), Active deformation of Asia: From kinematics to dynamics, *Science*, *278*(5338), 647–650, doi:10.1126/science.278.5338.647.

Ergintav, S., S. McClusky, E. Hearn, R. Reilinger, R. Cakmak, T. Herring, H. Ozener, O. Lenk, and E. Tari (2009), Seven years of postseismic deformation following the 1999, $M = 7.4$ and $M = 7.2$, Izmit-Duzce, Turkey earthquake sequence, *J. Geophys. Res.*, *114*, B07403, doi:10.1029/2008JB006021.

Fujiwara, T., S. Kodaira, T. No, Y. Kaiho, N. Takahashi, and Y. Kaneda (2011), The 2011 Tohoku-Oki earthquake: Displacement reaching the trench axis, *Science*, *334*(6060), 1240–1240, doi:10.1126/science.1211554.

Gephart, J. W. (1994), Topography and subduction geometry in the central Andes: Clues to the mechanics of a noncollisional orogen, *J. Geophys. Res.*, *99*(B6), 12,279–12,288, doi:10.1029/94JB00129.

Giraudo, R., and R. Limachi (2001), Pre-Silurian control in the genesis of the central and southern Bolivian fold belt, *J. South Am. Earth Sci.*, *14*, 665–680, doi:10.1016/S0895-9811(01)00068-2.

Gubbels, T. L., B. L. Isacks, and E. Farrar (1993), High-level surfaces, plateau uplift, and foreland development, Bolivian central Andes, *Geology*, *21*(8), 695–698.

Hackl, M., R. Malservisi, U. Hugentobler, and R. Wonnacott (2011), Estimation of velocity uncertainties from GPS time series: Examples from the analysis of the South African TrigNet network, *J. Geophys. Res.*, *116*, B11404, doi:10.1029/2010JB008142.

Hayes, G. P., M. W. Herman, W. D. Barnhart, K. P. Furlong, S. Riquelme, H. M. Benz, E. Bergman, S. Barrientos, P. S. Earle, and S. Samsonov (2014), Continuing megathrust earthquake potential in Chile after the 2014 Iquique earthquake, *Nature*, *512*(7514), 295–298, doi:10.1038/nature13677.

Hearn, E. H. (2003), What can GPS data tell us about the dynamics of post-seismic deformation?, *Geophys. J. Int.*, *155*(3), 753–777, doi:10.1111/j.1365-246X.2003.02030.x.

Herring, T. (2000), Documentation for GLOBK: Global Kalman Filter VLBI and GPS analysis program edited, MIT.

Hilley, G. E., and M. R. Strecker (2004), Steady state erosion of critical Coulomb wedges with applications to Taiwan and the Himalaya, *J. Geophys. Res.*, *109*, B01411, doi:10.1029/2002JB002284.

Horton, B. K. (1999), Erosional control on the geometry and kinematics of thrust belt development in the central Andes, *Tectonics*, *18*(6), 1292–1304, doi:10.1029/1999TC900051.

Hoth, S., J. Adam, N. Kukowsi, and O. Oncken (2007), Influence of erosion on the kinematics of bivergent orogens: Results from scaled sandbox simulations, in *Tectonics, Climate, and Landscape Evolution*, edited by S. D. Willett et al., *Geol. Soc. Am. Spec. Pap.*, *398*, pp. 201–225.

Houseman, G., and P. England (1986), Finite strain calculations of continental deformation: 1. Method and general results for convergent zones, *J. Geophys. Res.*, *91*(B3), 3651–3663, doi:10.1029/JB091iB03p03651.

Hsu, Y. J., M. Simons, S. B. Yu, L. C. Kuo, and H. Y. Chen (2003), A two-dimensional dislocation model for interseismic deformation of the Taiwan mountain belt, *Earth Planet. Sci. Lett.*, *211*(3–4), 287–294, doi:10.1016/s0012-821x(03)00203-6.

Hubbard, J., S. Barbot, E. M. Hill, and P. Tapponnier (2015), Coseismic slip on shallow décollement megathrusts: Implications for seismic and tsunami hazard, *Earth Sci. Rev.*, *141*(0), 45–55.

Hubbard, J., and J. H. Shaw (2009), Uplift of the Longmen Shan and Tibetan plateau, and the 2008 Wenchuan ($M = 7.9$) earthquake, *Nature*, *458*, doi:10.1038/nature07837.

Isacks, B. L. (1988), Uplift of the central Andean Plateau and bending of the Bolivian orocline, *J. Geophys. Res.*, *93*(B4), 3211–3231, doi:10.1029/JB093iB04p03211.

Kanamori, H. (1977), The energy release in great earthquakes, *J. Geophys. Res.*, *82*, 2981–2987, doi:10.1029/JB082i020p02981.

Kao, H., and W. P. Chen (2000), The Chi-Chi earthquake sequence: Active, out-of-sequence thrust faulting in Taiwan, *Science*, *288*(5475), 2346–2349, doi:10.1126/science.288.5475.2346.

Kendrick, E., M. Bevis, R. J. Smalley, and B. A. Brooks (2001), An integrated crustal velocity field for the central Andes, *Geochem. Geophys. Geosyst.*, *2*, 1066, doi:10.1029/2001GC000191.

Kendrick, E., M. Bevis, R. J. Smalley, B. A. Brooks, R. B. Vargas, E. Lauría, and L. P. S. Fortes (2003), The Nazca-South America Euler vector and its rate of change, *J. South Am. Earth Sci.*, *16*(2), 125–131.
Kendrick, E., B. A. Brooks, M. Bevis, R. Smalley Jr., E. Lauria, M. Araujo, and H. Parra (2006), Active orogeny of the South-Central Andes studied with GPS geodesy, *Rev. Asoc. Geol. Argent.*, *61*(4), 555–566.
Kendrick, E. C., M. Bevis, R. F. Smalley Jr., O. Cifuentes, and F. Galban (1999), Current rates of convergence across the central Andes: Estimates from continuous GPS observations, *Geophys. Res. Lett.*, *26*(5), 541–544, doi:10.1029/1999GL900040.
King, R., and Y. Bock (2000), *Documentation for the GAMIT GPS Analysis Software*, edited by MIT and Scripps Inst. of Oceanogr, Cambridge, Mass.
Kley, J. (1996), Transition from basement-involved to thin-skinned thrusting in the Cordillera Oriental of southern Bolivia, *Tectonics*, *15*(4), 763–775, doi:10.1029/95TC03868.
Lamb, S. (2000), Active deformation in the Bolivian Andes, South America, *J. Geophys. Res.*, *105*(B11), 25,627–625,653, doi:10.1029/2000JB900187.
Lamb, S., and E. Smith (2013), The nature of the plate interface and driving force of interseismic deformation in the New Zealand plate-boundary zone, revealed by the continuous GPS velocity field, *J. Geophys. Res. Solid Earth*, *118*, 3160–3189, doi:10.1002/jgrb.50221.
Langbein, J. (2004), Noise in two-color electronic distance meter measurements revisited, *J. Geophys. Res.*, *109*, B04406, doi:10.1029/2003JB002819.
Langbein, J. (2012), Estimating rate uncertainty with maximum likelihood: Differences between power-law and flicker–random-walk models, *J. Geod.*, *86*(9), 775–783, doi:10.1007/s00190-012-0556-5.
Langbein, J., and H. Johnson (1997), Correlated errors in geodetic time series: Implications for time-dependent deformation, *J. Geophys. Res.*, *102*(B1), 591–603, doi:10.1029/96JB02945.
Lavé, J., and J. P. Avouac (2000), Active folding of fluvial terraces across the Siwalik Hills (Himalaya of central Nepal), *J. Geophys. Res.*, *105*, 5735–5770, doi:10.1029/1999JB900292.
Lay, T., and S. Bilek (2007), Anomalous earthquake ruptures at shallow depths on subduction zone megathrusts, in *The Seismogenic Zone of Subduction Thrust Faults*, edited by T. H. Dixon and J. C. Moore, pp. 476–511, Columbia Univ. Press, New York.
Lay, T., et al. (2005), The great Sumatra-Andaman earthquake of 26 December 2004, *Science*, *308*(5725), 1127–1133, doi:10.1126/science.1112250.
Leturmy, P., J. L. Mugnier, P. Vinour, P. Baby, B. Colletta, and E. Chabron (2000), Piggyback basin development above a thin-skinned thrust belt with two detachment levels as a function of interactions between tectonic and superficial mass transfer: The case of the Subandean Zone (Bolivia), *Tectonophysics*, *320*(1), 45–67, doi:10.1016/S0040-1951(00)00023-8.
Lin, Y. N. N., et al. (2013), Coseismic and postseismic slip associated with the 2010 Maule Earthquake, Chile: Characterizing the Arauco Peninsula barrier effect, *J. Geophys. Res. Solid Earth*, *118*, 3142–3159, doi:10.1002/jgrb.50207.
Lindsey, E. O., R. Natsuaki, X. Xu, M. Shimada, M. Hashimoto, D. Melgar, and D. T. Sandwell (2015), Line-of-sight displacement from ALOS-2 interferometry: M_w 7.8 Gorkha earthquake and M_w 7.3 aftershock, *Geophys. Res. Lett.*, *42*, 6655–6661, doi:10.1002/2015GL065385.
Mao, A. L., C. G. A. Harrison, and T. H. Dixon (1999), Noise in GPS coordinate time series, *J. Geophys. Res.*, *104*(B2), 2797–2816, doi:10.1029/1998JB900033.
Mary, B. C. L., B. Maillot, and Y. M. Leroy (2013a), Deterministic chaos in frictional wedges revealed by convergence analysis, *Int J Numer Anal Met Geomechanics*, *37*(17), 3036–3051, doi:10.1002/nag.2177.
Mary, B. C. L., B. Maillot, and Y. M. Leroy (2013b), Predicting orogenic wedge styles as a function of analogue erosion law and material softening, *Geochem. Geophys. Geosyst.*, *14*, 4523–4543, doi:10.1002/ggge.20262.
Masek, J. G., B. L. Isacks, T. L. Gubbels, and E. J. Fielding (1994), Erosion and tectonics at the margins of continental plateaus, *J. Geophys. Res.*, *99*(B7), 13,941–913,956, doi:10.1029/94JB00461.
McQuarrie, N. (2002), The kinematic history of the central Andean fold-thrust belt, Bolivia: Implications for building a high plateau, *Geol. Soc. Am. Bull.*, *114*(8), 950–963.
McQuarrie, N., T. A. Ehlers, J. B. Barnes, and B. Meade (2008), Temporal variation in climate and tectonic coupling in the central Andes, *Geology*, *36*(12), 999–1002.
McQuarrie, N., B. K. Horton, G. Zandt, S. Beck, and P. G. DeCelles (2005), Lithospheric evolution of the Andean fold-thrust belt, Bolivia, and the origin of the central Andean Plateau, *Tectonophysics*, *399*(1–4), 15–37.
Meade, B. J., Y. Klinger, and E. A. Hetland (2013), Inference of multiple earthquake-cycle relaxation timescales from irregular geodetic sampling of interseismic deformation, *Bull. Seismol. Soc. Am.*, *103*(5), 2824–2835, doi:10.1785/0120130006.
Menke, W. (1989), *Geophysical Data Analysis: Discrete Inverse Theory*, 289 pp., Academic Press, San Diego, Calif.
Moreno, M., M. Rosenau, and O. Oncken (2010), 2010 Maule earthquake slip correlates with pre-seismic locking of Andean subduction zone, *Nature*, *467*(7312), 198–U184, doi:10.1038/Nature09349.
Mugnier, J.-L., D. Becel, and D. Granjeon (2006), Active tectonics in the Subandean belt inferred from the morphology of the Rio Pilcomayo (Bolivia), *GSA Special Paper*, *398*, 353–369, doi:10.1130/2006.2398(15).
Norabuena, E., L. Leffler-Griffin, A. Mao, T. Dixon, S. Stein, I. S. Sacks, L. Ocola, and M. Ellis (1998), Space geodetic observations of Nazca-South America convergence across the central Andes, *Science*, *279*(5349), 358–362.
Okada, Y. (1985), Surface deformation due to shear and tensile faults in a half-space, *Bull. Seismol. Soc. Am.*, *75*, 1135–1154.
Poblet, J., and R. J. Lisle (2011), *Kinematic Evolution and Structural Styles of Fold-and-Thrust Belts*, 255 pp., Williston, VT, Geological Society, Bath, U. K.
Reilinger, R., et al. (2006), GPS constraints on continental deformation in the Africa-Arabia-Eurasia continental collision zone and implications for the dynamics of plate interactions, *J. Geophys. Res.*, *111*, B05411, doi:10.1029/2005JB004051.
Rocha, E., and E. O. Cristallini (2015), Controls on structural styles along the deformation front of the Subandean zone of southern Bolivia, *J. Struct. Geol.*, *73*(0), 83–96, doi:10.1016/j.jsg.2015.02.010.
Sapkota, S. N., L. Bollinger, Y. Klinger, P. Tapponnier, Y. Gaudemer, and D. Tiwari (2013), Primary surface ruptures of the great Himalayan earthquakes in 1934 and 1255, *Nat. Geosci.*, *6*(1), 71–76.
Savage, J. C. (1983), A dislocation model of strain accumulation and release at a subduction zone, *J. Geophys. Res.*, *88*(B6), 4984–4996, doi:10.1029/JB088iB06p04984.
Scholz, C. H. (1988), The brittle-plastic transition and the depth of seismic faulting, *Geol. Rundsch.*, *77*(1), 319–328, doi:10.1007/bf01848693.
Scholz, C. J. (1998), Earthquakes and friction laws, *Nature*, *391*, 37–42.
Schurr, B., et al. (2014), Gradual unlocking of plate boundary controlled initiation of the 2014 Iquique earthquake, *Nature*, *512*(7514), 299–302, doi:10.1038/nature13681.

Schurr, B., G. Asch, M. Rosenau, R. Wang, O. Oncken, S. Barrientos, P. Salazar, and J. P. Vilotte (2012), The 2007 *M*7.7 Tocopilla northern Chile earthquake sequence: Implications for along-strike and downdip rupture segmentation and megathrust frictional behavior, *J. Geophys. Res.*, *117*, B05305, doi:10.1029/2011JB009030.

Segall, P., and J. L. Davis (1997), GPS applications for geodynamics and earthquake studies, *Annu. Rev. Earth Planet. Sci.*, *25*, 301–336, doi:10.1146/Annurev.Earth.25.1.301.

Simoes, M., J. P. Avouac, and Y. G. Chen (2007), Slip rates on the Chelungpu and Chushiang thrust faults inferred from a deformed strath terrace along the Dungpuna River, west central Taiwan, *J. Geophys. Res.*, *112*(B3), doi:10.1029/2005JB004200.

Simons, M. (2007), Interferometric synthetic aperture radar geodesy, in *Treatise on Geophysics*, edited by G. Schubert, pp. 351–390.

Strecker, M. R., R. N. Alonso, B. Bookhagen, B. Carrapa, G. E. Hilley, E. R. Sobel, and M. H. Trauth (2007), Tectonics and climate of the southern central Andes, *Annu. Rev. Earth Planet. Sci.*, *35*, 747–787.

Suppe, J., and D. Medwedeff (1990), Geometry and kinematics of fault-propagation folding, *Eclogae Geol. Helv.*, *83*(3), 409–454.

Tobita, M. (2016), Combined logarithmic and exponential function model for fitting postseismic GNSS time series after 2011 Tohoku-Oki earthquake, *Earth Planets Space*, *68*(1), 1–12, doi:10.1186/s40623-016-0422-4.

Tregoning, P., R. Burgette, S. C. McClusky, S. Lejeune, C. S. Watson, and H. McQueen (2013), A decade of horizontal deformation from great earthquakes, *J. Geophys. Res. Solid Earth*, *118*, 2371–2381, doi:10.1002/jgrb.50154.

Uba, C. E., C. Heubeck, and C. Hulka (2006), Evolution of the late Cenozoic Chaco foreland basin, southern Bolivia, *Basin Res.*, *18*(2), 145–170.

Uba, C. E., J. Kley, M. Strecker, and A. K. Schmitt (2009), Unsteady evolution of the Bolivian Subandean thrust belt: The role of enhanced erosion and clastic wedge progradation, *Earth Planet. Sci. Lett.*, *281*, 134–146.

Vergne, J., R. Cattin, and J. P. Avouac (2001), On the use of dislocations to model interseismic strain and stress build-up at intracontinental thrust faults, *Geophys. J. Int.*, *147*, 155–162.

Vigny, C., et al. (2005), Insight into the 2004 Sumatra-Andaman earthquake from GPS measurements in southeast Asia, *Nature*, *436*(7048), 201–206, doi:10.1038/nature03937.

Vigny, C., et al. (2011), The 2010 M_w 8.8 Maule megathrust earthquake of Central Chile, monitored by GPS, *Science*, *332*(6036), 1417–1421, doi:10.1126/science.1204132.

Wang, K. L., Y. Hu, and J. H. He (2012), Deformation cycles of subduction earthquakes in a viscoelastic Earth, *Nature*, *484*(7394), 327–332, doi:10.1038/nature11032.

Weiss, J. R., B. A. Brooks, J. R. Arrowsmith, and G. Vergani (2015), Spatial and temporal distribution of deformation at the front of the Andean orogenic wedge in southern Bolivia, *J. Geophys. Res. Solid Earth*, *120*, 1909–1931, doi:10.1002/2014JB011763.

Wessel, P., W. H. F. Smith, R. Scharroo, J. Luis, and F. Wobbe (2013), Generic Mapping Tools: Improved version released, *Eos Trans. AGU*, *94*(45), 409–410, doi:10.1002/2013EO450001.

Whipple, K. X. (2009), The influence of climate on the tectonic evolution of mountain belts, *Nat. Geosci.*, *2*, doi:10.1038/ngeo413.

Whipple, K. X., and B. J. Meade (2004), Controls on the strength of coupling among climate, erosion, and deformation in two-sided, frictional orogenic wedges at steady state, *J. Geophys. Res.*, *109*, 24, doi:10.1029/2003JF000019.

Williams, S. D. P. (2003), The effect of coloured noise on the uncertainties of rates estimated from geodetic time series, *J. Geod.*, *76*(9–10), 483–494, doi:10.1007/S00190-002-0283-4.

Williams, S. D. P., Y. Bock, P. Fang, P. Jamason, R. M. Nikolaidis, L. Prawirodirdjo, M. Miller, and D. J. Johnson (2004), Error analysis of continuous GPS position time series, *J. Geophys. Res.*, *109*(B3), doi:10.1029/2003JB002741.

Wright, T. J. (2002), Remote monitoring of the earthquake cycle using satellite radar interferometry, *Philos. Trans. Math. Phys. Eng. Sci.*, *360*(1801), 2873–2888, doi:10.2307/3558932.

Yagupsky, D., B. A. Brooks, K. X. Whipple, C. C. Duncan, and M. Bevis (2014), Distribution of active faulting along orogenic wedges: Minimum-work models and natural analogue, *J. Struct. Geol.*, *66*, 237–247.

Ye, L., T. Lay, H. Kanamori, and K. Koper (2015), Rapidly estimated seismic source parameters for the 16 September 2015 Illapel, Chile M_w 8.3 earthquake, *Pure Appl. Geophys.*, *173*(2), 1–12, doi:10.1007/s00024-015-1202-y.

Yue, L.-F., J. Suppe, and J.-H. Hung (2005), Structural geology of a classic thrust belt earthquake: The 1999 Chi-Chi earthquake Taiwan (M_w = 7.6), *J. Struct. Geol.*, *27*(11), 2058–2083.

Zhang, J., Y. Bock, H. Johnson, P. Fang, S. Williams, J. Genrich, S. Wdowinski, and J. Behr (1997), Southern California Permanent GPS Geodetic Array: Error analysis of daily position estimates and site velocities, *J. Geophys. Res.*, *102*(B8), 18,035–18,055, doi:10.1029/97JB01380.